Solar Physics (2023) 298:112
https://doi.org/10.1007/s11207-023-02207-5

RESEARCH

Magnetic Field and Plasma Diagnostics for Solar Coronal Mass Ejections: A Case Study Using the Forward Modeling Approach

X. Liu[1] · H. Tian[1,2] · T. Török[3] · S. Gibson[4] · Z. Yang[1] · W. Li[5] · T. Samanta[6]

Received: 11 April 2023 / Accepted: 10 September 2023
© The Author(s), under exclusive licence to Springer Nature B.V. 2023

Abstract

The proposed *COronal Solar Magnetism Observatory* (COSMO) *Large Coronagraph* (LC) will provide unique observations to study coronal mass ejections (CMEs) with its ability to diagnose the magnetic field and plasma properties in the solar corona. In this article, we take a realistic magnetohydrodynamic CME model and synthesize the signals of several coronal emission lines (CELs) to perform a forward modeling of COSMO LC observations of a CME. We use the Stokes parameters of the Fe XIII 10747 Å line to diagnose the magnetic field and plasma properties of the CME flux rope. The results show that COSMO LC can provide magnetic field measurements of CME progenitors with a high spatial resolution (pixel size $= 2''$). During a CME eruption, the COSMO LC observations may be used to qualitatively study the evolution of the magnetic field using a lower spatial resolution (pixel size $= 6''$). We then use the synthetic signals of several other CELs to diagnose the physical conditions in the CME leading front, including the shock. The COSMO LC observations of the Fe XIII 10798/10747 Å and Ni XV 8026/6703 Å line pairs could provide density diagnostics of the front. By observing several CELs with different formation temperatures, the COSMO LC could be used to diagnose the temperature and ionization states in the front. We suggest that the Fe XIII 10747 Å line should be given the highest priority when observing CMEs, while observations of the Fe XIII 10798 Å, Fe XIV 5303 Å, and Fe XV 7062 Å lines, and the Ni XV 8026/6703 Å line pair can also provide valuable information on CMEs.

✉ H. Tian
huitian@pku.edu.cn

1 School of Earth and Space Sciences, Peking University, Beijing 100871, China

2 Key Laboratory of Solar Activity and Space Weather, National Space Science Center, Chinese Academy of Sciences, Beijing 100190, China

3 Predictive Science Inc., 9990 Mesa Rim Road, Suite 170, San Diego, CA 92121, USA

4 High Altitude Observatory, National Center for Atmospheric Research, 3080 Center Green Drive, Boulder, CO 80301, USA

5 National Astronomical Observatories, Chinese Academy of Sciences, Beijing 100012, China

6 Indian Institute of Astrophysics, Koramangala, Bangalore 560034, India

Published online: 03 October 2023

Keywords Magnetohydrodynamic simulations · Solar coronal mass ejections · Coronagraphic imaging · Solar coronal lines · Solar magnetic fields

1. Introduction

Coronal mass ejections (CMEs) are regarded as the most spectacular eruptive events in the solar system (e.g. Chen, 2011; Webb and Howard, 2012). CMEs carry an immense amount of plasma and magnetic flux away from the Sun at a typical speed of several hundred km s^{-1} and the fastest speed of over 3000 km s^{-1} in extreme cases (e.g. Yashiro et al., 2004). The significance of understanding such events is magnified by their later impact on the Earth. When interplanetary CMEs interact with the Earth's magnetosphere in the form of magnetic clouds, severe geomagnetic storms could be triggered, which can cause damage to human society (e.g. Burlaga et al., 1982; Schrijver, 2015). Improving our understanding of CMEs' triggering mechanisms, structure, and propagation is one of the major goals of space weather studies.

CMEs have been observed by various kinds of instruments. White-light coronagraphs such as the *Large Angle and Spectrometric Coronagraph* (LASCO: Brueckner et al., 1995) on board the *Solar and Heliospheric Observatory* (SOHO: Domingo, Fleck, and Poland, 1995) and the COR1 and COR2 coronagraphs on board the *Solar TErrestrial RElations Observatory* (STEREO: Kaiser et al., 2008) have played important roles in CME observations. Through the measurements of polarized or total brightness of white light in large fields of view (FOVs), the white-light coronagraphs can provide information on the origin, propagation, and physical properties of CMEs (e.g. Wang et al., 2002; Lin et al., 2005; Zhou, Wang, and Wang, 2006; Vourlidas et al., 2010; Ying et al., 2019). Statistical investigations of CMEs were carried out using these large FOV coronagraphs (e.g. Gopalswamy et al., 2010b,a; Vourlidas et al., 2013). Narrow-band imaging at extreme-ultraviolet (EUV) wavelengths is another approach to study CMEs. The *Extreme-ultraviolet Imaging Telescope* (EIT: Delaboudinière et al., 1995) on board SOHO started the era to study the EUV waves generated by CMEs (e.g. Thompson et al., 1998; Biesecker et al., 2002; Chen et al., 2002; Attrill et al., 2007). In recent years, the *Atmospheric Imaging Assembly* (AIA: Lemen et al., 2012) on board the *Solar Dynamics Observatory* (SDO: Pesnell, Thompson, and Chamberlin, 2012) has provided temperature diagnostics of CMEs with high-resolution observations of emission lines formed over a wide temperature range (e.g. Cheng et al., 2012; Hou et al., 2022). Other approaches, such as observations of CME-induced radio bursts (e.g. Gopalswamy et al., 2003; Liu et al., 2009; Su et al., 2022) and spectroscopic observations of EUV lines (e.g. Landi et al., 2010; Tian et al., 2012; Xu et al., 2022), have also contributed to CME studies.

Despite intensive investigations of CMEs based on the approaches mentioned above, many open questions remain. One of the core challenges for CME studies is to measure the coronal magnetic field. The coronal magnetic field governs CMEs from their energy build-up processes to their eruptions (e.g. Forbes, 2000; Karpen, Antiochos, and DeVore, 2012), but direct measurements of the coronal magnetic field are elusive. The coronal magnetic field measurements can be achieved in several ways, including using the Zeeman effects of visible and infrared spectral lines (e.g. Lin, Penn, and Tomczyk, 2000; Lin, Kuhn, and Coulter, 2004; Li, Landi Degl'Innocenti, and Qu, 2017), the coronal seismology diagnostics (e.g. Nakariakov and Ofman, 2001; Chen et al., 2010; Yang et al., 2020a,b), the magnetic-field-induced-transition method (Li et al., 2015, 2016; Chen et al., 2021, 2023; Landi et al., 2020), and through the unsaturated Hanle effect (e.g. Fineschi et al., 1993; Raouafi et al., 2016;

Zhao et al., 2019, 2021). The Zeeman-effect measurement is generally well understood and routinely used to infer photospheric magnetic fields (e.g. Scherrer et al., 2012), yet applying this method to coronal measurements is still challenging due to the weak field strength (≈ 1 G) and the faint emission (0.1 – 10 parts per million (ppm) of the solar disk center intensity for the Stokes I emission) in the corona. The *Solar Observatory for Limb Active Regions and Coronae* (SOLARC: Kuhn et al., 2003) and the *Coronal Multi-channel Polarimeter* (CoMP: Tomczyk et al., 2008) were designed to measure the coronal magnetic fields through the Zeeman and Hanle effects, but their capabilities to measure CME-associated magnetic fields are limited by the long exposure times relative to the dynamic time scales of CMEs.

Fortunately, the proposed *COronal Solar Magnetism Observatory* (COSMO: Tomczyk et al., 2016) *Large Coronagraph* (LC) has the potential to provide magnetic field measurements of CMEs. COSMO LC is a ground-based instrument designed to measure full Stokes parameters of the well-known Fe XIII 10747 Å and a list of other visible and infrared coronal emission lines (CELs). With its 1.5 m aperture, LC will observe the off-limb corona over a large 1° FOV (i.e. 1.05 – 2 $R_\odot$) with a spatial two-pixel resolution of 2″ and a temporal cadence of 1 s, and will measure the line of sight (LOS) component of the coronal magnetic field using Stokes V (circular polarization) signals. The Fe XIII 10747 Å line has a comparatively high sensitivity to the magnetic field (e.g. Querfeld, 1977; House, 1977). The linear polarization of this line is sensitive to the coronal magnetic field orientation due to the saturated Hanle effect (Sahal-Brechot, 1977), which has been used to infer coronal magnetic field topologies and diagnose the magnetic free energy (e.g. Dove et al., 2011; Rachmeler et al., 2013; Bak-Steslicka et al., 2013; Jibben, Reeves, and Su, 2016; Chen et al., 2018; Gibson et al., 2017; Corchado-Albelo et al., 2021). Apart from the magnetic field measurements, COSMO LC will also provide diagnostics of the plasma condition. LC will observe other CELs formed at different temperatures, for example, the coronal green line (Fe XIV 5303 Å) and the coronal red line (Fe X 6374 Å). Several density-sensitive line pairs will also be included for density measurements.

Besides COSMO LC, some other instruments will provide similar observations. For instance, the upgraded CoMP (UCoMP: Tomczyk and Landi, 2019) can observe the CELs in a similar way as COSMO LC, although its aperture (20 cm) is much smaller than that of COSMO LC. The *Visible Emission Line Coronagraph* (VELC: Raghavendra Prasad et al., 2017) on board the proposed *Aditya*-L1 mission (Seetha and Megala, 2017) will observe the Fe XIII 10747 Å line in space with higher efficiency than ground-based instruments. The *Cryogenic Near-Infrared Spectro-Polarimeter* (Cryo-NIRSP: Fehlmann et al., 2023) designed for the *Daniel K. Inouye Solar Telescope* (DKIST: Rimmele et al., 2020) will also measure the full Stokes parameters of several CELs at wavelengths from 1 to 5 μm with a 4 m aperture and a relatively smaller 5′ FOV.

The incoming instruments raise the demand for a better understanding of the CEL observations of CMEs. This paper aims to investigate what we can learn about CMEs with COSMO LC observations and provide possible guidance for future observations through a forward modeling approach. In this work, we use a CME model and simulate the COSMO LC observations of CEL signals from this CME. Our CME model, CEL synthesis, and methodology will be described in Section 2. Section 3 presents our synthesized results. In Section 4, we study the potential of the instrument to diagnose the magnetic field and the plasma properties in the CME. We discuss the potential of COSMO LC in CME studies in Section 5. Our conclusions are summarized in Section 6.

2. Methods

2.1. CME Model

The CEL signals produced by CMEs critically depend on the plasma environment of the CME, which means that a realistic CME model is needed for the CEL synthesis. The model used in this work is a 3D MHD simulation of the 2000 July 14 Bastille Day eruption event from Török et al. (2018). The construction of the model was based on the Magnetohydrodynamic Algorithm outside a Sphere (MAS: Lionello, Linker, and Mikić, 2009) code from Predictive Science Inc. This model successfully reproduced several observational features of the real Bastille Day event and has been used for several CME studies (e.g. Reginald, Newmark, and Rastaetter, 2020; Young et al., 2021).

The construction of the model was divided into two steps. The first was to construct a steady background corona. The input magnetogram for the model was composed of a SOHO *Michelson Doppler Imager* (MDI: Scherrer et al., 1995) synoptic photospheric magnetogram for Carrington rotation (CR) 1965 combined with an MDI full-disk magnetogram for active region NOAA 9077. The model evolved for 160 Alfvén times ($1\tau_A \approx 24$ min) under the equations and heating functions similar to those in Lionello, Linker, and Mikić (2009). We note that recent MAS simulations used the turbulence of propagating Alfvén waves to drive coronal heating (Mikić et al., 2018). After a steady-state corona model was obtained, the next step was to simulate the CME eruption. By inserting seven overlapping modified Titov–Démoulin (TDm; Titov et al., 2014) flux ropes with different strengths, orientations, and heights, the model reproduced a flux rope with a morphology as suggested by the observations of the flare arcade and the pre-eruptive filament. The configuration was then thermodynamically relaxed for $2\tau_A$. After this, a convergence flow was imposed in the inner boundary for another $2\tau_A$, which finally triggered the eruption at $t = 164\tau_A$. A fast-mode shock wave was formed during the propagation, as will be seen in Section 3. We refer to Török et al. (2018) for a detailed description of the model.

For the purpose of our analysis, we reset $t = 0$ to the onset of the CME eruption (i.e. $t = 164\tau_A$ before the resetting) throughout the text below. We extracted the data at 26 different moments starting from $t = 0.00$ to $t = 12$ min with a temporal interval of approximately 29 s. Note that this was the optimal uniform temporal interval available from the simulation. During this period, the CME material has propagated through a distance of several solar radii. Figure 1 shows some snapshots from the model. Panels a and b are the synthesized SDO/AIA 304 Å images at $t = 0$ min and $t = 4.32$ min, respectively. Panels c and d show the CME flux rope and its magnetic field strength distributions for the two moments, respectively. Panel e shows the polar view of the CME flux rope and our assumed LOS in a sketch. Although the Bastille Day eruption headed towards the Earth, we choose a different viewing angle so that the CME is placed off-limb.

2.2. CELs Synthesis

We simulated the observations of several CELs in the candidate line list for COSMO LC. Table 1 shows the CELs used in this work, along with their wavelengths and formation temperatures (i.e. the temperature of maximum ionization fraction assuming ionization equilibrium). These lines provide a temperature coverage from $\log T/\mathrm{K} \approx 6.25$ to ≈ 6.65. Four density-sensitive line pairs, i.e. the Fe XIII 10747/10798 Å, Ni XV 8026/6703 Å, Ar XIII 10143/8300 Å, and Ca XV 5694/5445 Å, are included in this list. It is essential to note that the Ar XIII 10143 and 8300 Å lines have not been detected yet, which highlights the

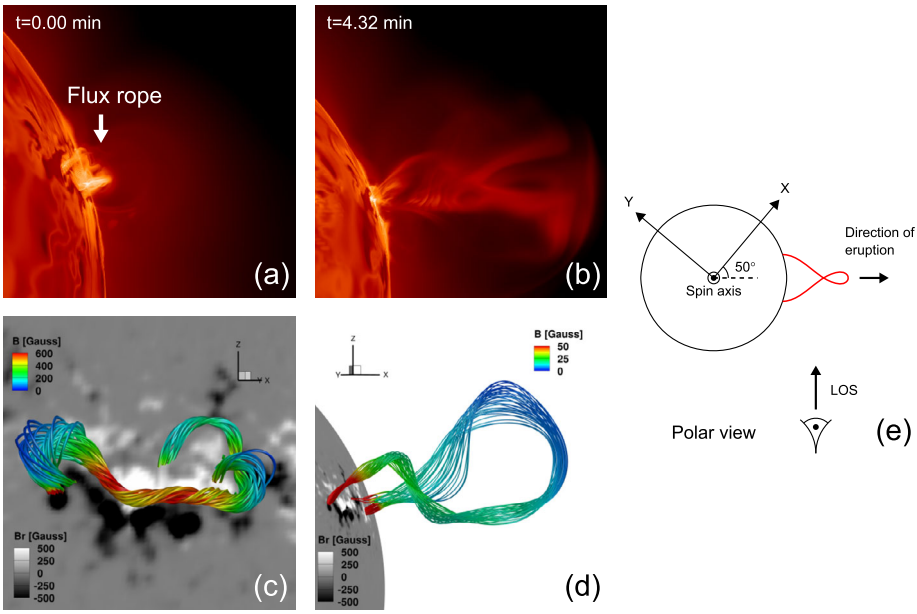

Figure 1 (**a**) Synthesized SDO/AIA 304 Å intensity image of the CME flux rope at $t = 0$. (**b**) Similar to (**a**), but at $t = 4.32$ min. (**c**) Configuration of the flux rope at $t = 0$ and the photospheric radial magnetogram. The color of field lines represents magnetic field strength. (**d**) Similar to (**c**), but at $t = 4.32$ min and from another viewing angle. (**e**) A sketch of the CME eruption and the LOS viewed from above the North Pole.

Table 1 Ions, wavelengths, and formation temperatures of CLEs.

Ion	wvl [Å]	$\log T_f$/K
Fe XIII	10747	6.25
Fe XIII	10798	6.25
Fe XIV	5303	6.3
Fe XV	7062	6.35
Ni XV	6703	6.4
Ni XV	8026	6.4
Ar XIII	10143	6.45
Ar XIII	8300	6.45
Ca XV	5694	6.65
Ca XV	5445	6.65

importance of conducting forward modeling to gain a better understanding before future observations. It should be mentioned that these lines are also in the candidate line list for UCoMP (Landi, Habbal, and Tomczyk, 2016).

We first synthesized Stokes signals of the Fe XIII 10747 Å line using the Coronal Line Emission (CLE; Judge and Casini, 2001) code embedded in the FORWARD package (Gibson et al., 2016). The CLE code was developed for the synthesis of Stokes parameters of CELs from plasma and magnetic field conditions along the LOS. At each pixel in the image, we calculated the profile of each Stokes parameter (I_λ, Q_λ, U_λ, and V_λ, each as a function

of the wavelength λ) of the Fe XIII 10747 Å line. Since COSMO LC will use tunable filters to receive signals at different wavelengths, the wavelength range is limited compared with slit spectrometers. We used a wavelength range from 10742.3 to 10750.0 Å, which corresponds to a range from ≈ -100 to ≈ 100 km s^{-1} in terms of Doppler shift. This short range inevitably led to the consequence that the signals from plasma with high speed may not be received. Nevertheless, we found that this did not severely affect the synthetic features that we are interested in. In order to exactly obtain the Stokes parameters, the profiles were nonuniformly sampled at 100 wavelengths with a minimum wavelength interval of 0.045 Å. Note that this interval is much smaller than the typical value of instruments using tunable filters (e.g. 1.1 Å for UCoMP). After obtaining the profiles of the Stokes parameters, we first applied the Gaussian fitting to the Stokes I profile and derived the central wavelength λ_0 and e-folding line width Γ (which equals $\frac{1}{2\sqrt{\ln 2}}$ FWHM) of the profile. Then, the total intensities of Stokes parameters, i.e. (I, Q, U, V), were calculated as

$$(I, Q, U, V) = \int (I_\lambda, Q_\lambda, U_\lambda, \mathrm{sgn}(\lambda - \lambda_0) V_\lambda) d\lambda. \tag{1}$$

Here $\mathrm{sgn}(\lambda - \lambda_0)$ means the sign of $\lambda - \lambda_0$. We then used $L = \sqrt{Q^2 + U^2}$ to represent the total linear polarization magnitude. The plane-of-sky (POS) azimuth of magnetic the field, Az, was calculated as $Az = \frac{1}{2} \arctan \frac{U}{Q}$.

For other lines in this study, we only synthesized the intensity images. We first used the CHIANTI database (version 10.0.1; Dere et al., 1997; Del Zanna et al., 2021) to calculate the contribution functions of these lines. Since the emission of these lines results from both collisional and radiative excitation processes, we considered the photoexcitation caused by photospheric radiation. In this way, we expressed each contribution function as a function of plasma temperature T, electron density N_e, and heliocentric distance r. We calculated the contribution functions at a large number of $\log T/\mathrm{K}$ (from $\log T_f/\mathrm{K}-0.5$ to $\log T_f/\mathrm{K}+0.5$ with a step of 0.02), $\log N_e/\mathrm{cm}^{-3}$ (from 5.0 to 13.0 with a step of 0.1), and $r/R_\odot$ (from 1.0 to 3.0 with a step of 0.01). The coronal element abundances we used were from Schmelz et al. (2012). For each LOS, we chose ≈ 600 points with a uniform step of $0.005 R_\odot$, and calculated the emissivities of lines by interpolating the contribution functions for the local values of $\log T/\mathrm{K}$, $\log N_e/\mathrm{cm}^{-3}$, and $r/R_\odot$. The total intensities of the lines were derived by integrating the signals along the LOS. We excluded points with LOS velocities higher than 100 km s^{-1} for consistency with Fe XIII 10747Å synthesis.

When synthesizing these lines, we ignored the time required for ionization equilibrium in the CME plasma. The impact will be discussed in Section 3.

2.3. Diagnostic Methods

2.3.1. Magnetic Field Diagnostic Method

Here we briefly introduce our method to infer the LOS magnetic field from the synthesized signals. Because of the Zeeman effect, the Stokes V of Fe XIII 10747Å can be used to measure the LOS component of the magnetic field (B_{LOS}). Our method to measure B_{LOS} and estimate the uncertainty comes from Fan, Gibson, and Tomczyk (2018). This B_{LOS} is expressed as

$$B_{LOS} = \frac{\sqrt{\pi}}{2} \frac{\Gamma}{k} \frac{V}{I}, \tag{2}$$

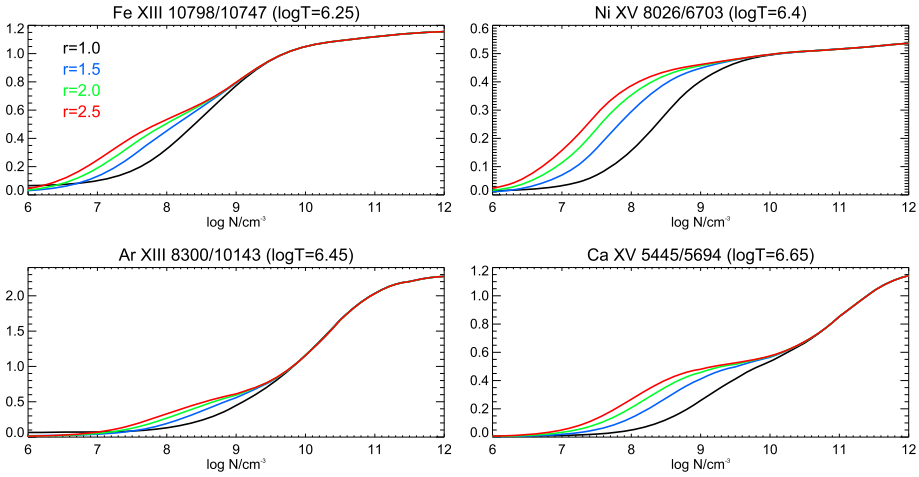

Figure 2 Intensity ratios of the density-sensitive line pairs. Each ratio is a function of density and heliocentric distance.

here Γ is the e-folding line width of Stokes I profile in nm and $k = 8.1 \times 10^{-6}$ nm/G is the Zeeman sensitivity of the Fe XIII 10747 Å line. The relative uncertainty of B_{LOS} caused by photon counting error, $U_r(B_{LOS})$, can be estimated by

$$U_r(B_{LOS}) = \frac{1}{\epsilon_V}\frac{I}{V}\frac{\sqrt{\Phi_I + 2\Phi_s}}{\Phi_I}, \tag{3}$$

where $\epsilon_V = 1/\sqrt{3}$ denotes the modulation efficiency for Stokes V. Also Φ_I and Φ_s are the photon numbers of Stokes I signal and scatter light, respectively; Φ_I is related to Γ, the telescope aperture D, the system efficiency ϵ, the pixel size δx, and the exposure time δt (see equation 7 in Fan, Gibson, and Tomczyk, 2018). We used the assumption in Fan, Gibson, and Tomczyk (2018) that the intensity of scattered light is 5 ppm. In this way, we estimated Φ_s using the solar disk center intensity. The solar disk center intensity was calculated by the IDL function "for_sun_flux" in the FORWARD package.

In this paper, D and ϵ were set to 1.5 m and 0.0943 (Tomczyk 2015, private communication), respectively, based on the proposed settings of COSMO LC. To simulate the observations with different resolutions and exposure times, we used various values of δx and δt for different situations, as will be seen in Section 4.

2.3.2. Density Diagnostic Method

We used the Fe XIII 10798/10747 Å, Ni XV 8026/6703 Å, Ar XIII 8300/10143 Å, and Ca XV 5445/5694 Å density-sensitive line pairs synthesized with CHIANTI for density diagnostics. Using the contribution functions we derived with CHIANTI in Section 2.2, the intensity ratio of each line pair is written as a function of T, N_e, and r. When measuring the density using each line pair, we assumed the temperature to be the formation temperature of each line pair. The heliocentric distance r for each pixel was assumed to be the distance between the solar center and the LOS corresponding to this pixel. Figure 2 shows the intensity ratios each as a function of $\log N_e$ and r. The density could thus be determined given the intensity ratio and heliospheric distance.

We also investigated the uncertainty of the measured density caused by photon noise. To do this, we first wrote the measured density as $N_e = N_e(a, r)$, where $a = I_1/I_2$ represents the intensity ratio of two lines in a line pair. Differentiating N_e and a gives

$$\sigma_{N_e} = \frac{\partial N_e}{\partial a}\frac{I_1}{I_2}\sqrt{(\frac{\sigma_{I_1}}{I_1})^2 + (\frac{\sigma_{I_2}}{I_2})^2}, \tag{4}$$

where σ_{N_e}, σ_{I_1}, and σ_{I_2} are uncertainties of N_e, I_1, and I_2, respectively. The term $\frac{\partial N_e}{\partial a}$ can be calculated theoretically. The relative uncertainty of the intensity can be estimated by Φ_I and Φ_s as $\frac{\sigma_I}{I} = \frac{1}{\sqrt{\Phi_I}}\sqrt{1 + 2\frac{\Phi_s}{\Phi_I}}$, which further gives

$$U_r(N_e) = \frac{1}{N_e}\frac{\partial N_e}{\partial a}\frac{I_1}{I_2}\sqrt{\frac{\Phi_{I_1} + 2\Phi_{s_1}}{\Phi_{I_1}^2} + \frac{\Phi_{I_2} + 2\Phi_{s_2}}{\Phi_{I_2}^2}}. \tag{5}$$

Here $U_r(N_e) = \frac{\sigma_N}{N}$ is the relative uncertainty of the measured density. In this study, we assumed that the scattered light intensity for each line is 5 ppm (Fan, Gibson, and Tomczyk, 2018). Similar to the calculation in Section 2.3.1, we calculated Φ_I and Φ_s, and used Equation 5 to estimate $U_r(N_e)$.

3. Synthetic Results

Figure 3a–e shows the synthetic results of Fe XIII 10747 Å at $t = 0$. We also plot the magnetic field, temperature, and density in the POS cross-section, as shown in Figure 3f–h. In each panel, we mask the region below $1.05R_\odot$, which is the edge of the COSMO occulter. The black arrow in the Fe XIII 10747 Å intensity image marks the flux rope structure, which is characterized by a strong magnetic field strength (≈ 600 G), low temperature ($10^{5-5.5}$ K), and high density ($\approx 10^{10}$ cm^{-3}). Since the formation temperature of the Fe XIII 10747 Å line is much higher than the temperature in the core of the flux rope, the strong intensity is mainly produced by the material at the boundary between the flux rope and external field. The bright rings around the flux rope indicate the external strapping field. Figure 3b shows the map of the linear polarization degree. One can notice the weak linear polarization degree in the flux rope, which is because the magnetic field is nearly parallel to the LOS in the flux rope (as shown in Figure 1c). A "lagomorphic" signature is also visible in the linear polarization degree image. According to Rachmeler et al. (2013), this "lagomorphic" signature is produced by the flux-rope magnetic field configuration. The CoMP observations have also revealed similar structures (Bak-Steslicka et al., 2013; Chen et al., 2018).

Figure 3c shows a significant enhancement of line width in the strapping fields around the core of the flux rope. This enhancement was first noticed by Tian et al. (2013) in CoMP observations of CMEs. They explained that such enhancement is caused by the inhomogeneous plasma motions along the LOS. Figure 3d shows several arch-shaped signatures in Doppler velocity. These arch-shaped signatures are possibly caused by plasma flows along magnetic field lines (e.g. Schmit et al., 2009; Bak-Steslicka, Gibson, and Chmielewska, 2016; Chen et al., 2018)

Figure 4 shows the results and physical quantities in the model at $t = 2.88$ min. At this moment, a shock wave was formed due to the high velocity of the plasma. We plotted the contour of $\nabla \cdot v = -0.05$ (i.e. a strong compression of the plasma) in the POS in each

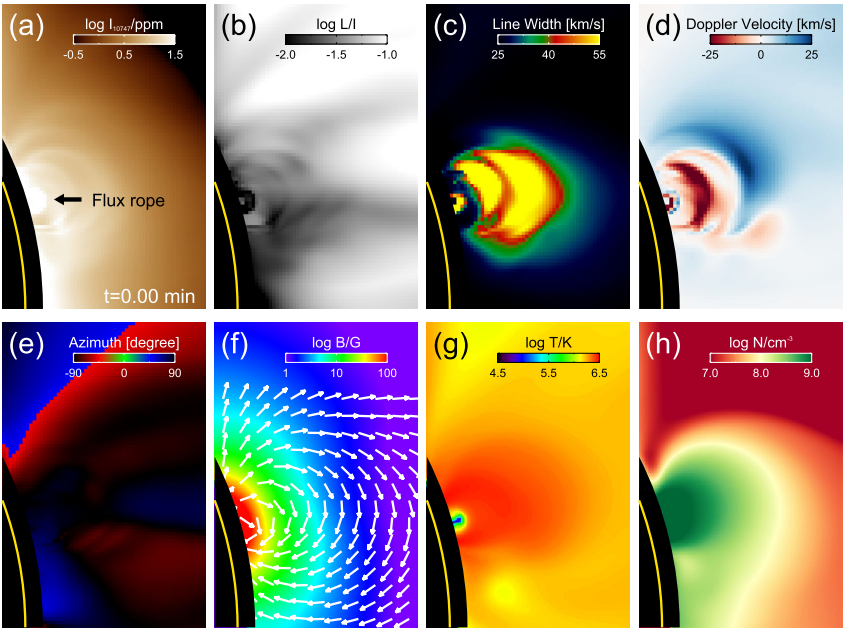

Figure 3 Synthesized results of the Fe XIII 10747 line, along with several POS cross-section quantities in the model at $t = 0$. (**a**)–(**e**) Intensity (Stokes I), linear polarization degree (L/I), line width, Doppler velocity, and radial azimuth derived from synthesized signals. (**f**)–(**h**) Magnetic field, temperature, and density distributions in the POS. The solar disk is indicated by the yellow curve in each panel. The region below $1.05R_\odot$ is masked.

panel of Figure 4 to represent the shock location. It should be stressed that this only outlines the intersection between the shock wave and POS, thus some of the shock-wave-associated signals from other cross-sections may slightly fall outside the contour. To present some detailed information on the shock, we selected two cuts in Figure 4g for further analysis. Our analysis is similar to that in Jin, Nitta, and Cohen (2022). The upper three rows in Figure 5 present the distribution of the magnetic field, velocity, and density along the two cuts. Based on these curves, we determined the boundaries of the shock wave on both the upstream and downstream sides, as shown by the dashed lines in each panel. The magnetic field and velocity magnitudes both experienced a decline from downstream to upstream. By taking the upstream and downstream magnetic field vectors, we calculated the coplanarity normal **n** (e.g. Lepping and Argentiero, 1971) of the wavefront as

$$\mathbf{n} = \pm \frac{(\mathbf{B}_u \times \mathbf{B}_d) \times (\mathbf{B}_u - \mathbf{B}_d)}{|(\mathbf{B}_u \times \mathbf{B}_d) \times (\mathbf{B}_u - \mathbf{B}_d)|}. \tag{6}$$

Here u and d denote upstream and downstream, respectively. We determined the electron density N_e and the normal velocity v_n in the upstream and downstream, and calculated the local normal velocity of the shock as

$$v_{n,s} = \frac{N_{e,u} v_{n,d} - N_{e,d} v_{n,u}}{N_{e,u} - N_{e,d}}. \tag{7}$$

We then obtained the normal velocity relative to the shock $v_n'(= v_n - v_{n,s})$ as blue curves in the fourth row in Figure 5. We also calculated the fast-mode speed v_f as red curves, from

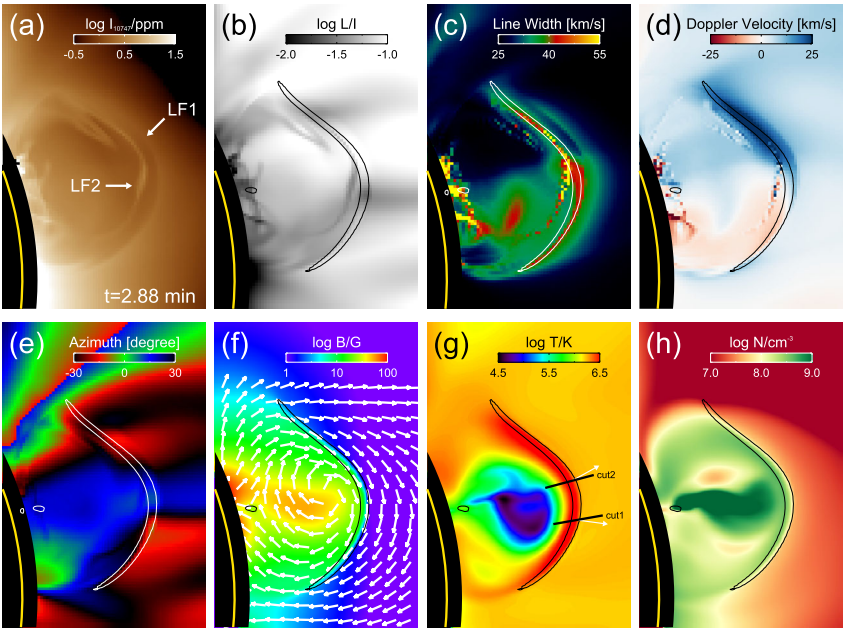

Figure 4 Similar to Figure 3 but at $t = 2.88$ min. The arc-shaped contour in each panel represents $\nabla \cdot v = -0.05$. Two LFs can be distinguished in (**a**). We choose two cuts in (**g**) for detailed analysis of the shock in Figure 5. Each white arrow in (**g**) represents the POS projection of the deduced shock normals.

which one can learn that the fast-mode speed in the downstream is higher than that in the upstream. The last row in Figure 5 shows the Mach number (v_n'/v_f) profiles along the two cuts. The Mach number in the upstream is ≈ 3, while it decreases to ≈ 0 in the downstream. These properties suggest that this shock is a fast-mode shock.

Two leading fronts LF1 (along the shock wave) and LF2 (behind LF1) near the shock can be identified from Figure 4. The two leading fronts are produced by plasma with a temperature close to the formation temperature of the Fe XIII 10747 Å line. In the region between LF1 and LF2 (i.e. the region near the shock wave), the Fe XIII 10747 Å intensity is weak due to the high temperature in the shock (≈ 3 MK). The Fe XIII 10747 Å line width and Doppler velocity both experience a sudden change across the shock. In the shock downstream, the line width and Doppler velocity are both high due to the fast plasma motion. Figure 4e shows that the azimuth also changes significantly across the shock. Although the azimuth is determined by the linear polarization, we caution that the azimuth distribution cannot be used to directly infer the magnetic field direction due to the LOS integration effect and the 90° Van Vleck ambiguity.

Figure 6 presents the synthesized intensity images for several other lines. The patterns in the Fe XIV 5303 Å images are similar to those of Fe XIII 10747 Å due to their similar formation temperatures. The Fe XV 7062 Å, Ar XIII 10143 Å, and Ca XV 5694 Å lines have higher formation temperatures (> 2 MK) compared to the typical coronal temperature. As a result, their signals from the background plasma are faint, while their signals contributed by the CME plasma are strong due to the high temperature near and in the shock. Therefore, the wave leading front appears to be sharp in the intensity images of these three lines.

Our calculations above assumed that the plasma is in ionization equilibrium. However, the CME propagation timescale may be much shorter than the time required for ioniza-

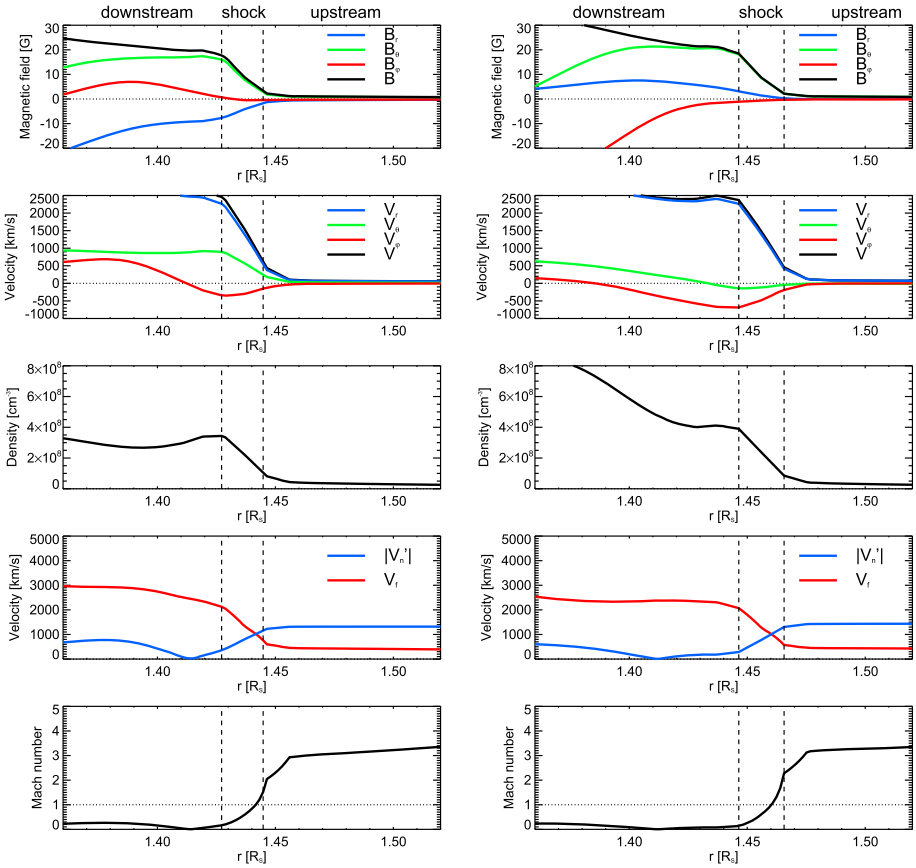

Figure 5 Magnetic field, velocity, density, normal velocity in the shock frame (v_n') and fast-mode speed (v_f), and Mach number profiles along the two cuts in Figure 4g.

tion equilibrium (Frassati, Mancuso, and Bemporad, 2020). The consequent nonequilibrium ionization may significantly affect the emissions (Dudík et al., 2017; Lee et al., 2019). To assess the influence of ignoring such an effect, we calculated the time scales for six ionization processes listed in Table 2 using a typical shock temperature $T = 3.0$ MK and density $N_e = 10^{8.5}$ cm^{-3} in our model. Our calculation is similar to that in Ma et al. (2011). We assumed that the ionization starts from Fe XII, Ni XI, Ar X, and Ca XI ions since their peak temperatures (1.6, 1.3, 1.4, and 1.3 MK, respectively) are close to the typical coronal temperature. Considering that the CME eruption starts at $t = 0$ while its leading front forms at around $t = 2.88$ min, we used 2.88 min as the propagation time scale of the CME. From Table 2, one can learn that the time scales for Fe to be ionized to Fe XIII, Fe XIV, and Fe XV, and the time scale for Ni to be ionized to Ni XV are much shorter than the CME propagation time scale. Therefore, the intensities of the Fe XIII 10747 Å, Fe XIV 5303 Å, Fe XV 7062 Å, and the Ni XV lines are not significantly affected by the ionization process. The ionization time scale of Ar XIII ions is comparable to the CME propagation time scale, which means that the intensities of Ar XIII lines are slightly overestimated. For the Ca XV lines, their intensities are severely overestimated since the CME propagation time scale is much shorter

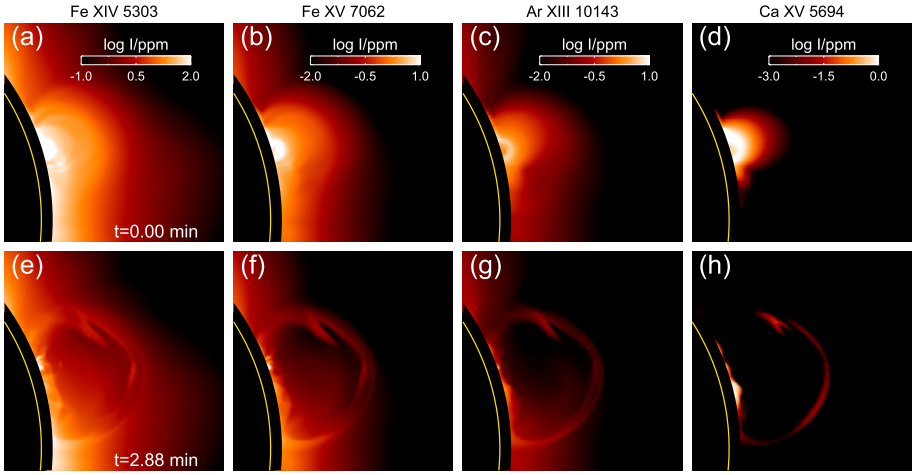

Figure 6 Intensity images of the Fe XIV 5303, Fe XV 7062, Ar XIII 10143, and Ca XV 5694 lines at $t = 0$ (upper row) and $t = 2.88$ min (lower row).

Table 2 Time scales of several ionization processes.

Ionization process	t [s]
Fe XII – Fe XIII	8.6
Fe XII – Fe XIV	20.9
Fe XII – Fe XV	40.6
Ni XI – Ni XV	45.3
Ar X – Ar XIII	128.0
Ca XI – Ca XV	497.7

than the ionization time scale of Ca XV. In Section 4, we will discuss the influence caused by the overestimation of intensities of Ar XIII and Ca XV lines.

4. Physical Parameter Diagnostics

4.1. Magnetic Field Measurements

To comprehensively explore the magnetic field diagnostics, we divide our investigation into two parts. First, we investigate the magnetic field measurements of a steady flux rope. Then, we discuss the magnetic field measurements of the erupting CME.

We first took the synthetic data at $t = 0$ to simulate the preeruption magnetic field diagnostics. As we mentioned above, a convergence flow at the inner boundary was used to trigger the eruption. Since the slow expansion of the flux rope induced by the converging flows was not yet part of the actual eruption, we assumed the velocity in the model to be zero at $t = 0$. A pixel size δx of $2''$ and an exposure time of 15 min were adopted. Our results of the magnetic field measurements are shown in Figure 7. Based on the synthesized Fe XIII 10747 Å Stokes V/I and Stokes I line width, we calculated the magnetic field strength, as shown in panel b. Panel c shows the relative uncertainty of the B_{LOS}. The contour in panel

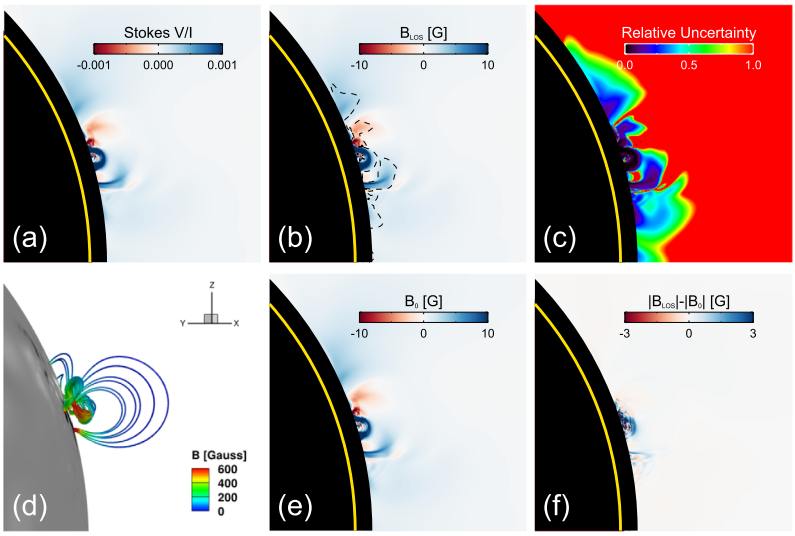

Figure 7 Magnetic field measurement of the flux rope before the eruption: (**a**) Stokes V/I, (**b**) B_{LOS} inferred from (**a**), (**c**) σB, (**d**) The flux rope and the strapping field lines, (**e**) B_0, i.e. the emissivity-weighted average LOS magnetic field, (**f**) The difference between the magnitudes of inferred B_{LOS} and B_0.

b marks out the region where $U_r(B_{LOS})$ is smaller than $\frac{1}{3}$. Panel d shows the magnetic field lines in the model. Comparing panels b and d, one sees that the inferred B_{LOS} map can reflect the flux rope and the strapping field structure in the model.

In order to quantitatively evaluate the inferred B_{LOS}, a parameter directly derived from the model is required. Due to the LOS integration effect, an LOS-averaged value of B_{LOS} can better match the physical meaning of the inferred B_{LOS} than the distribution of B_{LOS} in a cross section. To determine such a parameter, we start from the localized form of Equation 2, i.e.

$$B_{LOS,local} = \frac{\sqrt{\pi}}{2} \frac{\Gamma_{local}}{k} \frac{e_{V,local}}{e_{I,local}}, \tag{8}$$

which describes the relationship between the local magnetic field and the signals from local plasma. Here $B_{LOS,local}$, Γ_{local}, $e_{V,local}$, and $e_{I,local}$ denote the LOS component of the local magnetic field, the line width of the signal from the local plasma, the local Stokes V emissivity, and the local Stokes I emissivity of the Fe XIII 10747 Å line, respectively. Multiplying Equation 8 by $e_{I,local}$ and integrating it along the LOS gives

$$\int_{LOS} e_{I,local} B_{LOS,local} dl = \int_{LOS} \frac{\sqrt{\pi}}{2} \frac{\Gamma_{local}}{k} e_{V,local} dl. \tag{9}$$

To further reform Equation 9, we then assume that the line width Γ_{local} is roughly constant along the LOS. On the one hand, Γ_{local} can be moved outside the integral on the right-hand side. On the other hand, adopting this assumption implies that the measured intensities of Stokes I and V satisfy $\frac{V}{I} = \frac{\int_{LOS} e_{V,local} dl}{\int_{LOS} e_{I,local} dl}$, which, in other words, means that the Stokes I and V signals emitted from different LOS points are simply summed due to the invariant width and central wavelength. Combining Equations 2 and 9, and using the inferences above, we

obtain

$$B_{LOS} = \frac{\int_{LOS} e_{I,local} \cdot B_{LOS,local} dl}{\int_{LOS} e_{I,local} dl}. \tag{10}$$

Equation 10 shows that the measured B_{LOS} equals the emissivity weighted average value of $B_{LOS,local}$ along the LOS, if we assume first that the local line width is roughly constant along the LOS, and second that the Doppler velocity of the plasma is negligible. We thus use the right-hand side of Equation 10 to represent the magnetic field in the model (B_0), as is shown in panel e. Comparing Figures 7b and 7e, one can see that the general pattern of B_{LOS} is highly similar to that of B_0. Figure 7f shows the difference between the magnitudes of the inferred B_{LOS} and B_0. A typical value of $||B_{LOS}| - |B_0||$ is only 0.5 G, which is much smaller than a typical B_{LOS} magnitude (≈ 10 G).

We then generated the synthetic data at several moments for the simulation of the magnetic field measurements during the CME eruption. Different from the pre-eruption case, we took into consideration the plasma motion in this part, meaning that the velocity in the model was nonzero. To capture the dramatic evolution of the magnetic field, a much shorter exposure time is needed, which can lead to a significant reduction of the S/N (signal-to-noise) ratio since photon noise increases with decreasing exposure time. On the other hand, one can use a larger pixel size to gain more photons, thus offsetting the reduction of the S/N ratio. Therefore, we first synthesized the data with a pixel size of $2''$ and then resized the data with a pixel size of $6''$ by averaging. When estimating the uncertainty caused by photon counting noise, we assumed δx and δt to be $6''$ and 12 s, respectively. To briefly consider the evolution of the model during each exposure, we averaged the synthesized signals at two adjacent simulation time steps for each measurement.

The results of the magnetic field measurement, along with the comparison between B_{LOS} and B_0, are shown in Figure 8. The first panel in Figure 8 shows the magnitude of the inferred B_{LOS} with noise, i.e. $B_{LOS} \cdot (1 + U_r(B_{LOS})R)$. Here R is a random value from a Gaussian distribution with standard deviation of 1 and an average value of 0. One can learn from the results at different moments that the region with reasonably low noise shrinks with time. This is because the S/N ratio of the Fe XIII 10747 Å line decreases with the plasma ejection. Generally, the measurements are only valid in the lower corona ($1.05 - 1.2 R_\odot$).

The third and fourth columns (from the left) of Figure 8 show the difference between $|B_{LOS}|$ and $|B_0|$ and the histograms of the relative error $(|B_{LOS}| - |B_0|)/|B_0|$. One can see that the B_{LOS} deviates from B_0 in the during-eruption case, which is different from the result in the pre-eruption case. The cause for such a discrepancy between $|B_{LOS}|$ and $|B_0|$ is primarily due to the Doppler shifts of inhomogeneous plasma motions along the LOS. When several flows of plasma with different LOS velocities are overlapped in the LOS, their composite signals can result in more than one component in the Stokes profiles. We took the pixel centered on $(1.001, 0.283)$ at $t = 0$ in Figure 8 for a closer examination. Figure 9 presents the Stokes I and V profiles at this pixel, along with the profiles of several physical parameters along the LOS corresponding to this pixel. We identified two components (p_1 and p_2 for the left and right components, respectively) in the Stokes I profile as red dashed curves and derived the peak intensity, line width, and Doppler shift of each component through a double-Gaussian fit. We also plotted the single Gaussian fitting result as the blue dashed curve. The center of p_1 matches the center of the Stokes V profile. To find out the sources of p_1 and p_2, we focused on the peak in the emissivity profile, as is marked by the vertical dashed–dotted line in the right panel of Figure 9. The LOS velocity of this peak (31.8 km s^{-1}) is close to that of p_1, and the LOS magnetic field strength of this point (237

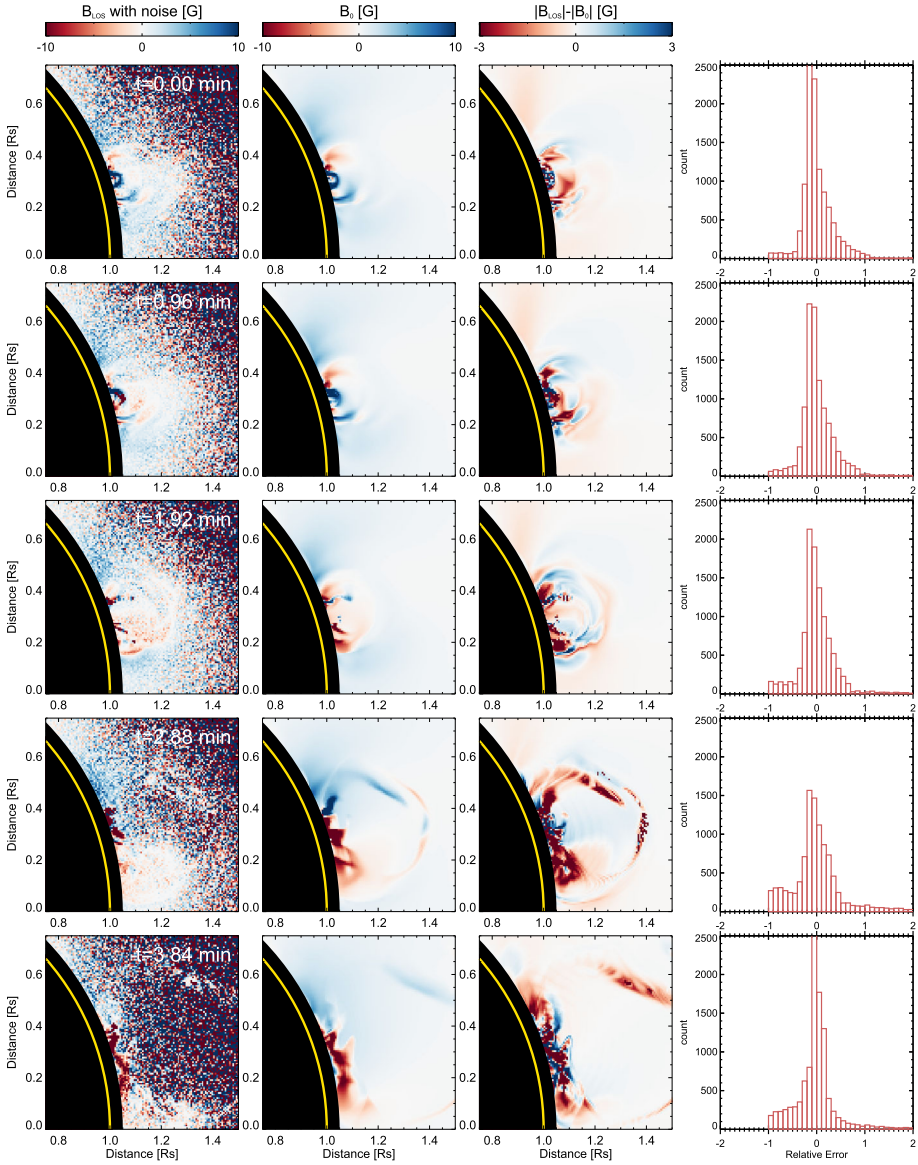

Figure 8 B_{LOS} diagnostics of the CME for $t = 0$ to 3.84 min: (first column) Inferred B_{LOS} with noise, (second column) B_0, (third column) The difference between inferred B_{LOS} and B_0, (last column) Histograms of $(|B_{LOS}| - |B_0|)/|B_0|$.

G) is also close to that inferred from p_1 and the Stokes V profile (228 G). This indicates that p_1 is produced by the region around the peak in the emissivity profile. At the same time, p_2 appears to be produced by the background plasma due to its low LOS velocity and weak corresponding signal in the Stokes V profile. These indicate that p_1 carries the information on the magnetic field in the flux rope, while p_2 only carries the information on the background plasma. Therefore, decomposition of p_1 and p_2 is required for the magnetic

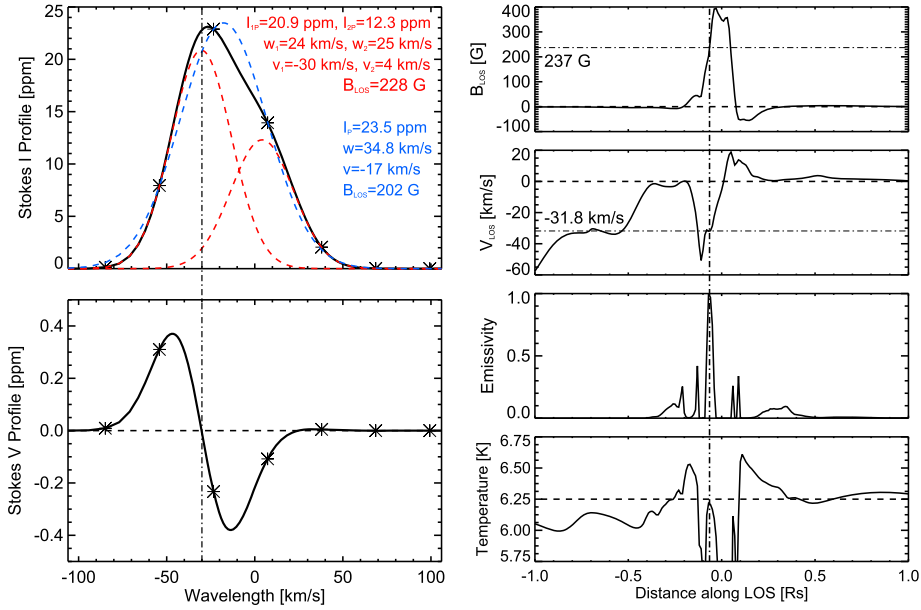

Figure 9 Stokes I and V profiles at the pixel located at $(1.001, 0.283)$ at $t = 0$ in Figure 8, and distributions of B_{LOS}, V_{LOS}, emissivity, and temperature along their corresponding LOS.

field measurement. Without such a decomposition, the B_{LOS} inferred from a single Gaussian fitting to the Stokes I profile is only 202 G, which significantly deviates from the actual field strength.

It can be deduced from the analysis above that the discrepancy between B_{LOS} and B_0 in Figure 8 is mainly caused by the undistinguished multiple components as a consequence of the CME eruption. Since COSMO LC will use tunable filters to obtain the profiles, the multiple components may not be distinguished in real observations due to the large sampling wavelength interval. We assume that the sampling wavelength interval is the same as that of UCoMP (1.1 Å), and marked the sampling wavelengths in the profiles in Figure 9. One can see that p_1 and p_2 cannot be easily decomposed, meaning that a precise measurement of the field strength in the erupting flux rope is difficult to realize.

One may also notice in Figure 9 that the inferred B_{LOS} ($\approx$ 200G) is only about half of the maximum B_{LOS} along the LOS (394 G). This is because the source region of p_1 does not locate at the region where B_{LOS} peaks. Due to the relatively weak B_{LOS} of this point and high temperature ($10^{6.25}$ K) compared to those in the flux rope, it can be deduced that the emissivity peak is located at the boundary between the flux rope and the background plasma. For the inner parts of the flux rope, i.e. the regions with peak B_{LOS}, the Fe XIII 10747 emissivity is weak due to the low temperature. Therefore, the measured B_{LOS} tends to be underestimated compared to the peak B_{LOS} in the flux rope. It should be noted that this underestimation is not caused by the plasma motion, thus it also exists when measuring the magnetic field of a steady flux rope. Fan, Gibson, and Tomczyk (2018) found a similar effect, which suggests that this underestimation can be universal.

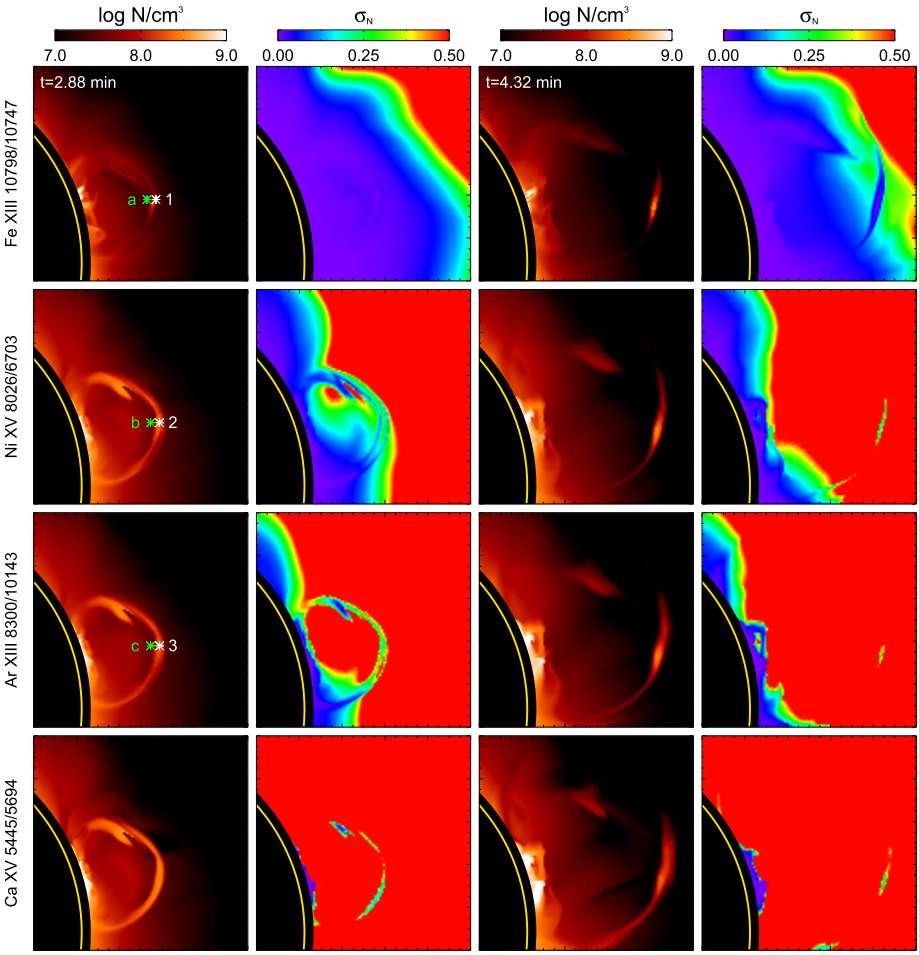

Figure 10 Density diagnostic results using four line pairs and the corresponding relative uncertainties. The first and second columns are for $t = 2.88$ min, while the third and fourth columns are for $t = 4.32$ min. The four rows represent results derived from the Fe XIII 10798/10747 Å, Ni XV 8026/6703 Å, Ar XIII 8300/10143 Å, and Ca XV 5445/5694 Å line pairs, respectively.

4.2. Density Diagnostics

In this section, we investigate the density diagnostics during the CME eruption. We took the synthetic data at $t = 2.88$ and $t = 4.32$ min for analysis. Similar to the magnetic field measurements, we ignored the evolution of the model during each exposure. Due to the fast motion of the CME leading front, we assumed the exposure time to be 4 s, and then modified the pixel size to $9''$. Figure 10 shows the density inferred from the four density-sensitive line pairs and the relative uncertainties $U_r(N_e)$ calculated using Equation 5. In the early stage of the eruption ($t = 2.88$ min), a clear leading front can be seen as an enhancement of the inferred density in each panel. At $t = 4.32$ min, the inferred density decreases as a result of the CME expansion.

Among the four line pairs, the Fe XIII 10798/10747 Å line pair has the highest S/N ratio, thus the Fe XIII 10798/10747 Å inferred density has the smallest uncertainty caused

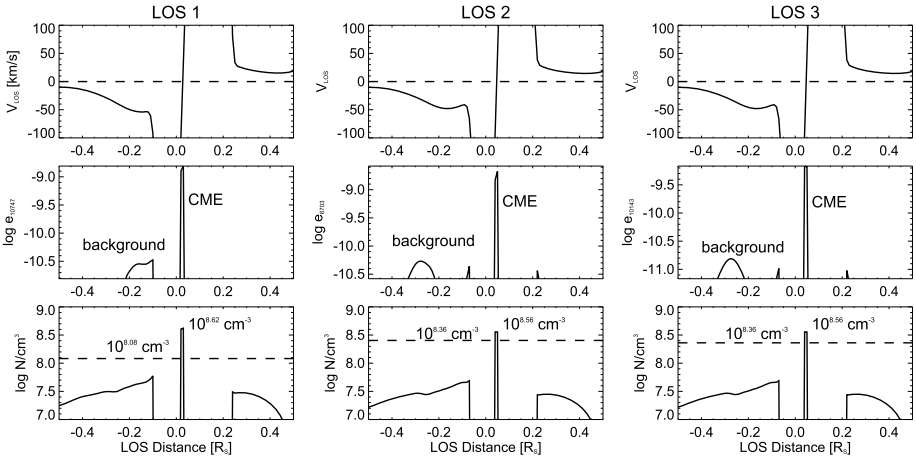

Figure 11 The distributions of LOS velocity, emissivity, and density along three LOSs. The dashed line in each panel of the last row indicates the inferred density without subtracting the background signals. The emissivity and density profiles only show parts where $|V_{LOS}| \leqslant 100$ km s^{-1}. LOS1, LOS2, and LOS3 correspond to pixel 1, 2, and 3 in Figure 10, respectively.

by photon counting. For the density inferred from the Ni XV 8026/6703 Å line pair, the uncertainty is also small enough for the density measurements in the shock front, although the uncertainty quickly increases with time, as one can see that the region where $U_r(N_e) < 1/3$ only takes a small fraction of the leading front at $t = 4.32$ min. The low S/N ratio of the Ar XIII 8300/10143 Å line pair results in a large uncertainty of the inferred density. At $t = 2.88$ min, the $U_r(N_e)$ of Ar XIII inferred density caused by photon counting is $\approx 1/3$ in the leading front, while at $t = 4.32$ min the uncertainty significantly increases. As has been discussed in Section 3, the intensities of the Ar XIII lines are slightly affected by the nonequilibrium ionization effect. Thus, the uncertainty of the density inferred from the Ar XIII line pair is expected to be even higher, which suggests that the density measurement based on the Ar XIII 8300/10143 Å line pair is valid only during the early stage of the eruption. Moreover, one may notice that the density maps inferred from the Ni XV and Ar XIII line pairs are similar, which is a result of the close peak temperatures of the two line pairs.

The density inferred from the Ca XV 5445/5694 Å line pair has the largest uncertainty. Due to our analysis in Section 3, the Ca XV strength of the signal is severely overestimated, thus the uncertainty of Ca XV 5445/5694 Å measured density can be even much larger. This indicates that the density measurement based on the Ca XV 5445/5694 Å line pair is unfeasible due to the low S/N.

To assess the density inferred from the Fe XIII, Ni XV and Ar XIII line pairs, we then chose three pixels (1, 2, 3) marked by the white asterisks in Figure 10 for a detailed analysis. The corresponding LOSs are dubbed as LOS1, LOS2, and LOS3, respectively. Figure 11 presents the distributions of LOS velocity, emissivity (the Fe XIII 10747 Å emissivity for LOS1, the Ni XV 6703 Å emissivity for LOS2, and the Ar XIII 10143 Å emissivity for LOS3, respectively) and density along the three LOSs. The points with LOS velocity higher than 100 km s^{-1} are removed since the signals from these points are out of the specified wavelength ranges. Each of the emissivity profiles shows a background component and a CME component, which indicates that the observed signals consist of both background sig-

nals and CME signals. As a consequence, the measured density is lower than the peak density along the LOS due to the averaging effect. The inferred densities for the three pixels are $10^{8.08}$, $10^{8.36}$, and $10^{8.36}$ cm^{-3}, respectively, which are smaller than the peak densities along the three LOSs ($10^{8.62}$, $10^{8.56}$, and $10^{8.56}$ cm^{-3}, respectively). We then attempted to correct the inferred densities of the two pixels by subtracting the background signals. We used the signals in the three pixels (a, b, c) marked by green asterisks in Figure 10 as the background signals. The inferred densities after subtracting the background signals are $10^{8.63}$, $10^{8.63}$, and $10^{8.59}$ cm^{-3}, respectively, which are closer to the peak densities along the LOSs compared with the densities inferred from raw signals. It should be mentioned that the error between inferred densities and peak densities along the LOSs still exists after the subtraction since the background signals cannot be accurately estimated by signals of other pixels. Despite this, the inferred densities are still close to the peak densities along the LOSs.

5. Discussion

5.1. Measuring the CME-Associated Magnetic Field

The CME progenitors are often characterized by flux rope structures (e.g. Vourlidas et al., 2013). Our investigation in Section 4.1 shows that COSMO LC can measure the LOS magnetic field strength of the stable flux rope with relatively small uncertainty caused by photon counting. In this work, a pixel size of 2″ was employed, which is much smaller than that in Fan, Gibson, and Tomczyk (2018) (12″). We found that the magnetic field strength is still measurable with high S/N ratio in a wide spatial range. This indicates that the high-resolution magnetic field maps from COSMO LC can help deduce the detailed structures of CME progenitors. Although the magnetic field measurements are affected by the LOS averaging effect, the strong correlation between the measured value and the emissivity-weighted field strength over the LOS gives us confidence for a quantitative analysis of the magnetic field structures of CME progenitors. We also found that the inferred magnetic field strength of the flux rope is approximately half of the LOS peak field strength, since the source region of the Fe XIII 10747 Å line locates at the boundary between the flux rope and the outer strapping field. Such an underestimation may be universal when observing flux ropes with thermal and magnetic structures similar to those of the flux rope in our model. Our results, together with those in Fan, Gibson, and Tomczyk (2018), can help us understand the COSMO LC measurements.

Our study also suggests that COSMO LC can diagnose the magnetic field during the CME eruption. By using a much larger pixel size, the magnetic field in the lower corona ($1 - 1.2R_{\odot}$) can be measured at a relatively fast cadence. In this work, an exposure time of 12 s is used, which indicates that a cadence of ≈ 1 min is needed for filters at five different wavelengths. A typical CME with a velocity of 400 – 500 km/s can propagate $\approx 3 \times 10^4$ km during such a cadence, which is much smaller than the solar radius (6.96×10^5 km). Therefore, COSMO LC will be able to capture the evolution of the large-scale magnetic field at least during the early stage of CME eruption. Meanwhile, the magnetic field measurements during CME eruptions are impacted by two factors. First, the fast expansion of CMEs can cause inhomogeneous plasma motions along the LOS, which may further lead to uncertainties in the inferred B_{LOS}. Second, the intensity of the Fe XIII 10747 line decreases with the ejection of plasma, which leads to a decrease of the S/N ratio. Despite these facts, the measurements can still provide qualitative information on the magnetic field of the erupting structure.

5.2. Diagnosing the CME Leading Front

Our results show that COSMO LC is capable of diagnosing the plasma properties in the CME shocks. The linear polarization signals, along with the line width and Doppler shift of the Fe XIII 10747 Å line, can be used to infer the morphology and the plasma motions in the CME leading front. Also, the leading front can be seen in intensity images of lines formed in a wide temperature range.

By using the Fe XIII 10798/10747 Å, Ni XV 8026/6703 Å, and Ar XIII 8300/10143 Å line pairs, COSMO LC can measure the density in the CME leading front. The density distributions inferred from the Ni XV 8026/6703 Å and Ar XIII 8300/10143 Å line pairs are similar due to their close peak temperatures. Considering that first the uncertainty of the density inferred from the Ar XIII 8300/10143 Å line pair is relatively large, and second the Ar XIII 8300/10143 Å line pair is yet to be observed, we suggest focusing on the Fe XIII 10798/10747 Å and Ni XV 8026/6703 Å line pairs for density measurements of the CME leading front.

Previously, the diagnostics of plasma properties in the CME shocks have been carried out based on SDO/AIA observations (e.g. Kozarev et al., 2011; Ma et al., 2011). The shock-associated leading fronts can be seen most clearly in AIA 193 Å (Fe XII, 1.4 MK) and 211 Å (Fe XIV, 2.0 MK) channels. AIA 335 Å (Fe XVI, 2.8 MK) channel also responds to the CME shocks, despite its relatively low S/N ratio. Compared with the diagnostics based on AIA observations, the diagnostics based on COSMO LC observations have several advantages. First, each of the AIA channels is contributed by lines formed at different temperatures (O'Dwyer et al., 2010), while the CELs observed by COSMO LC have much less blending. This means that the CEL signals can more precisely reflect the information on plasma at a specific temperature. Second, the density inferred from density-sensitive line pairs is less affected by the nonequilibrium ionization in the CME shocks. Using AIA observations, the density can be inferred from emission measure (EM) analysis. However, one has to assume an integration length along the LOS, which is often subject to a large uncertainty.

In addition, simultaneous observations of Fe XIII 10747 Å, Fe XIV 5303 Å, and Fe XV 7062 Å with COSMO LC will also help us understand the ionization processes in CME shocks.

5.3. Recommending CELs for CME Observations with COSMO

Here we compare the CELs we analyzed in terms of their potential to study CMEs. Among these CELs, Fe XIII 10747 Å should be given the highest priority when observing CMEs. First, the Stokes signals of Fe XIII 10747 Å can provide quantitative magnetic field measurements of CME progenitors and qualitative diagnostic of the magnetic field during CME eruption. When coupled with the Fe XIII 10798 Å line, the Fe XIII 10747 Å line can be used to measure the density in the CME leading front. Furthermore, the Fe XIII 10747 Å line provides diagnostics on the ionization processes in the CME leading front. We propose that the Fe XIV 5303 Å and Fe XV 7062 Å lines should also be included by COSMO LC, due to their ability to diagnose the temperature and ionization states in the CME leading front. It should be mentioned that the Stokes profiles of Fe XIV 5303 Å may also be helpful for magnetic field diagnostics (Mickey, 1973), although it is not discussed in this work.

We also recommend the Ni XV 8026/6703 Å line pair for density diagnostics of the CME leading front. Although the S/N ratio of this line pair is lower than that of the Fe XIII 10798/10747 line pair, we point out that one advantage of the Ni XV line pair is that its peak temperature (2.5 MK) is closer to the temperature of the shock front compared with

that of the Fe XIII 10798/10747 line pair (1.8 MK). The Ni XV signals from the CME shock is thus less affected by the background signals. One can learn from the analysis in Section 4.2 that the density inferred from the Fe XIII 10798/10747 significantly deviates from the density in the shock without subtracting the background signal, while for the Ni XV line pair the deviation is weaker. The Ar XIII 8300/10143 line pair could also provide similar measurements, although the uncertainty caused by photon counting is relatively large. We do not suggest including the Ca XV 5445 Å and 5694 Å lines in COSMO LC observations due to their low S/N ratios.

6. Conclusion

Based on a realistic MHD CME model, we have carried out a forward modeling of COSMO LC observation of a CME and investigated the potential of LC to diagnose the magnetic field and plasma properties of the CME. We have synthesized Stokes profiles of the Fe XIII 10747 Å line and intensity images of several other CELs. We then performed the magnetic field measurements of a steady flux rope and an erupting flux rope. Then, we performed the density measurements of the CME during its eruption. By calculating the uncertainties caused by the photon counting error and comparing the inferred quantities with model quantities, we discussed the feasibility of these measurements. At last, we concluded the potential of COSMO LC to study CMEs and discussed the priority of each CEL for CME observations.

Our conclusions are as follows:

1. The COSMO LC can reveal information on the detailed magnetic field structures in the CME progenitors by observing the Stokes parameters of the Fe XIII 10747 Å line with a high spatial resolution (2″ pixel size) and a relatively long exposure time (15 min). The measurements can be used to quantitatively study the magnetic field in the CME progenitors despite the LOS integration effect.
2. By using a lower resolution (6″ pixel size) and short exposure time (12 s), COSMO LC observations can help qualitatively understand the evolution of CME-associated magnetic field during the eruption. The magnetic field measurements can be affected by the inhomogeneous plasma motion in the CME.
3. COSMO LC can provide plasma diagnostics of the CME leading front. The linear polarization signals, line width, and Doppler shift of the Fe XIII 10747Å line carry information on the morphology and plasma motion of the CME shock. The Fe XIII 10798/10747 Å, Ni XV 8026/6703 Å, and Ar XIII 8300/10143 Å line pairs can provide density measurements of the CME leading front, and the former two have relatively higher S/N ratios. Observations of the Fe XIII 10747 Å, Fe XIV 5303 Å, and Fe XV 7062 Å lines can be used to study the ionization processes and temperature change in the CME leading front.
4. We suggest that the Fe XIII 10747 Å line should be given the highest priority in CME observations. The Fe XIII 10798 Å, Fe XIV 5303 Å, and Fe XV 7062 Å lines, and the Ni XV 8026/6703 Å line pair should be given secondary priority. We emphasize that this is from a perspective of a CME study.

Author contributions Xianyu Liu carried out the calculations and analysis, and wrote the first draft of the manuscript. Hui Tian conceived the idea, provided guidance on the study design, and revised the manuscript. Tibor Török provided the numerical model and gave suggestions on the calculations and manuscript writing. Sarah Gibson provided suggestions on the calculations and analysis and helped to revise the manuscript. Zihao Yang provided suggestions on the synthesized results and revised the manuscript. Wenxian Li provided part of atomic data and helped to revise the manuscript. Tanmoy Samanta provided critical feedback on the calculation and synthetic results. All authors reviewed the manuscript.

Funding This work is supported by the National Key R&D Program of China No. 2021YFA0718600, NSFC grant 12250006. This article is based upon work supported by the National Center for Atmospheric Research, which is a major facility sponsored by the National Science Foundation under Cooperative Agreement No. 1852977. We thank S. Tomczyk, E. Landi, and C. Downs for helpful discussions. We also thank B. Tremblay for an HAO internal review of this paper. We acknowledge support by ISSI-BJ to the team "Solar eruptions: Preparing for the next generation multi-waveband coronagraphs". T.T. acknowledges support from the HSR Program of NASA (Grant No. 80NSSC19K0858) and the Solar-Terrestrial Program of NSF (Grant No. AGS-1923377).

Declarations

Competing interests The authors declare no competing interests.

References

Attrill, G.D.R., Harra, L.K., van Driel-Gesztelyi, L., Démoulin, P.: 2007, Coronal "wave": magnetic footprint of a coronal mass ejection? *Astrophys. J. Lett.* **656**(2), L101. DOI. ADS.

Bak-Steslicka, U., Gibson, S., Chmielewska, E.: 2016, Line-of-sight velocity as a tracer of coronal cavity magnetic structure. *Front. Astron. Space Sci.* **3**, 7. DOI. ADS.

Bak-Steslicka, U., Gibson, S.E., Fan, Y., Bethge, C., Forland, B., Rachmeler, L.A.: 2013, The magnetic structure of solar prominence cavities: new observational signature revealed by coronal magnetometry. *Astrophys. J. Lett.* **770**(2), L28. DOI. ADS.

Biesecker, D.A., Myers, D.C., Thompson, B.J., Hammer, D.M., Vourlidas, A.: 2002, Solar phenomena associated with "EIT waves". *Astrophys. J.* **569**(2), 1009. DOI. ADS.

Brueckner, G.E., Howard, R.A., Koomen, M.J., Korendyke, C.M., Michels, D.J., Moses, J.D., Socker, D.G., Dere, K.P., Lamy, P.L., Llebaria, A., Bout, M.V., Schwenn, R., Simnett, G.M., Bedford, D.K., Eyles, C.J.: 1995, The Large Angle Spectroscopic Coronagraph (LASCO). *Solar Phys.* **162**(1–2), 357. DOI. ADS.

Burlaga, L.F., Klein, L., Sheeley, J.N.R., Michels, D.J., Howard, R.A., Koomen, M.J., Schwenn, R., Rosenbauer, H.: 1982, A magnetic cloud and a coronal mass ejection. *Geophys. Res. Lett.* **9**(12), 1317. DOI. ADS.

Chen, P.F.: 2011, Coronal mass ejections: models and their observational basis. *Living Rev. Solar Phys.* **8**(1), 1. DOI. ADS.

Chen, P.F., Wu, S.T., Shibata, K., Fang, C.: 2002, Evidence of EIT and Moreton waves in numerical simulations. *Astrophys. J. Lett.* **572**(1), L99. DOI. ADS.

Chen, Y., Song, H.Q., Li, B., Xia, L.D., Wu, Z., Fu, H., Li, X.: 2010, Streamer waves driven by coronal mass ejections. *Astrophys. J.* **714**(1), 644. DOI. ADS.

Chen, Y., Tian, H., Su, Y., Qu, Z., Deng, L., Jibben, P.R., Yang, Z., Zhang, J., Samanta, T., He, J., Wang, L., Zhu, Y., Zhong, Y., Liang, Y.: 2018, Diagnosing the magnetic field structure of a coronal cavity observed during the 2017 total solar eclipse. *Astrophys. J.* **856**(1), 21. DOI. ADS.

Chen, Y., Li, W., Tian, H., Chen, F., Bai, X., Yang, Y., Yang, Z., Liu, X., Deng, Y.: 2021, Forward modeling of solar coronal magnetic-field measurements based on a magnetic-field-induced transition in Fe X. *Astrophys. J.* **920**(2), 116. DOI. ADS.

Chen, Y., Li, W., Tian, H., Bai, X., Hutton, R., Brage, T.: 2023, Application of a magnetic-field-induced transition in Fe X to solar and stellar coronal magnetic field measurements. *Res. Astron. Astrophys.* **23**, 022001. DOI. ADS.

Cheng, X., Zhang, J., Saar, S.H., Ding, M.D.: 2012, Differential emission measure analysis of multiple structural components of coronal mass ejections in the inner corona. *Astrophys. J.* **761**(1), 62. DOI. ADS.

Corchado-Albelo, M.F., Dalmasse, K., Gibson, S., Fan, Y., Malanushenko, A.: 2021, Designing a new coronal magnetic field energy diagnostic. *Astrophys. J.* **907**(1), 23. DOI. ADS.

Del Zanna, G., Dere, K.P., Young, P.R., Landi, E.: 2021, CHIANTI—an atomic database for emission lines. XVI. Version 10, further extensions. *Astrophys. J.* **909**(1), 38. DOI. ADS.

Delaboudinière, J.-P., Artzner, G.E., Brunaud, J., Gabriel, A.H., Hochedez, J.F., Millier, F., Song, X.Y., Au, B., Dere, K.P., Howard, R.A., Kreplin, R., Michels, D.J., Moses, J.D., Defise, J.M., Jamar, C., Rochus, P., Chauvineau, J.P., Marioge, J.P., Catura, R.C., Lemen, J.R., Shing, L., Stern, R.A., Gurman, J.B., Neupert, W.M., Maucherat, A., Clette, F., Cugnon, P., Van Dessel, E.L.: 1995, EIT: extreme-ultraviolet imaging telescope for the SOHO mission. *Solar Phys.* **162**(1–2), 291. DOI. ADS.

Dere, K.P., Landi, E., Mason, H.E., Monsignori Fossi, B.C., Young, P.R.: 1997, CHIANTI – an atomic database for emission lines. *Astron. Astrophys. Suppl. Ser.* **125**, 149. DOI. ADS.

Domingo, V., Fleck, B., Poland, A.I.: 1995, The SOHO mission: an overview. *Solar Phys.* **162**(1-2), 1. DOI. ADS.

Dove, J.B., Gibson, S.E., Rachmeler, L.A., Tomczyk, S., Judge, P.: 2011, A ring of polarized light: evidence for twisted coronal magnetism in cavities. *Astrophys. J. Lett.* **731**(1), L1. DOI. ADS.

Dudík, J., Dzifčáková, E., Meyer-Vernet, N., Del Zanna, G., Young, P.R., Giunta, A., Sylwester, B., Sylwester, J., Oka, M., Mason, H.E., Vocks, C., Matteini, L., Krucker, S., Williams, D.R., Mackovjak, Š.: 2017, Nonequilibrium processes in the solar corona, transition region, flares, and solar wind (invited review). *Solar Phys.* **292**(8), 100. DOI. ADS.

Fan, Y., Gibson, S., Tomczyk, S.: 2018, The eruption of a prominence-carrying coronal flux rope: forward synthesis of the magnetic field strength measurement by the COronal solar magnetism observatory large coronagraph. *Astrophys. J.* **866**(1), 57. DOI. ADS.

Fehlmann, A., Kuhn, J.R., Schad, T.A., Scholl, I.F., Williams, R., Agdinaoay, R., Berst, D.C., Craig, S.C., Giebink, C., Goodrich, B., Hnat, K., James, D., Lockhart, C., Mickey, D.L., Oswald, D., Puentes, M.M., Schickling, R., de Vanssay, J.-B., Warmbier, E.A.: 2023, The Daniel K. Inouye Solar Telescope (DKIST) cryogenic near-infrared spectro-polarimeter. *Solar Phys.* **298**(1), 5. DOI. ADS.

Fineschi, S., Hoover, R.B., Zukic, M., Kim, J., Walker, J.A.B.C., Baker, P.C.: 1993, Polarimetry of HI Lyman-alpha for coronal magnetic field diagnostics. In: Hoover, R.B., Walker, J.A.B.C. (eds.) *Multilayer and Grazing Incidence X-Ray/EUV Optics for Astronomy and Projection Lithography*, *SPIE C.S.* **1742**, 423. DOI. ADS.

Forbes, T.G.: 2000, A review on the genesis of coronal mass ejections. *J. Geophys. Res.* **105**(A10), 23153. DOI. ADS.

Frassati, F., Mancuso, S., Bemporad, A.: 2020, Estimate of plasma temperatures across a CME-driven shock from a comparison between EUV and radio data. *Solar Phys.* **295**(9), 124. DOI. ADS.

Gibson, S., Kucera, T., White, S., Dove, J., Fan, Y., Forland, B., Rachmeler, L., Downs, C., Reeves, K.: 2016, FORWARD: a toolset for multiwavelength coronal magnetometry. *Front. Astron. Space Sci.* **3**, 8. DOI. ADS.

Gibson, S.E., Dalmasse, K., Rachmeler, L.A., De Rosa, M.L., Tomczyk, S., de Toma, G., Burkepile, J., Galloy, M.: 2017, Magnetic nulls and super-radial expansion in the solar corona. *Astrophys. J. Lett.* **840**(2), L13. DOI. ADS.

Gopalswamy, N., Shimojo, M., Lu, W., Yashiro, S., Shibasaki, K., Howard, R.A.: 2003, Prominence eruptions and coronal mass ejection: a statistical study using microwave observations. *Astrophys. J.* **586**(1), 562. DOI. ADS.

Gopalswamy, N., Akiyama, S., Yashiro, S., Mäkelä, P.: 2010b, Coronal mass ejections from sunspot and non-sunspot regions. In: *Magnetic Coupling Between the Interior and Atmosphere of the Sun*, *Astrophys. Space Sci. Proc.* **19**, 289. DOI. ADS.

Gopalswamy, N., Yashiro, S., Michalek, G., Xie, H., Mäkelä, P., Vourlidas, A., Howard, R.A.: 2010a, A catalog of halo coronal mass ejections from SOHO. *Sun Geosph.* **5**(1), 7. ADS.

Hou, Z., Tian, H., Wang, J.-S., Zhang, X., Song, Q., Zheng, R., Chen, H., Chen, B., Bai, X., Chen, Y., He, L., Song, K., Zhang, P., Hu, X., Dun, J., Zong, W., Song, Y., Xu, Y., Tan, G.: 2022, Three-dimensional propagation of the global extreme-ultraviolet wave associated with a solar eruption on 2021 October 28. *Astrophys. J.* **928**(2), 98. DOI. ADS.

House, L.L.: 1977, Coronal emission-line polarization from the statistical equilibrium of magnetic sublevels. I. Fe XIII. *Astrophys. J.* **214**, 632. DOI. ADS.

Jibben, P.R., Reeves, K.K., Su, Y.: 2016, Evidence for a magnetic flux rope in observations of a solar prominence-cavity system. *Front. Astron. Space Sci.* **3**, 10. DOI. ADS.

Jin, M., Nitta, N.V., Cohen, C.M.S.: 2022, Assessing the influence of input magnetic maps on global modeling of the solar wind and CME-driven shock in the 2013 April 11 event. *Space Weather* **20**(3), e2021SW002894. DOI. ADS.

Judge, P.G., Casini, R.: 2001, A synthesis code for forbidden coronal lines. In: Sigwarth, M. (ed.) *Advanced Solar Polarimetry – Theory, Observation, and Instrumentation*, *Astron. Soc. Pacific C.S.* **236**, 503. ADS.

Kaiser, M.L., Kucera, T.A., Davila, J.M., St. Cyr, O.C., Guhathakurta, M., Christian, E.: 2008, The STEREO mission: an introduction. *Space Sci. Rev.* **136**(1-4), 5. DOI. ADS.

Karpen, J.T., Antiochos, S.K., DeVore, C.R.: 2012, The mechanisms for the onset and explosive eruption of coronal mass ejections and eruptive flares. *Astrophys. J.* **760**(1), 81. DOI. ADS.

Kozarev, K.A., Korreck, K.E., Lobzin, V.V., Weber, M.A., Schwadron, N.A.: 2011, Off-limb solar coronal wavefronts from SDO/AIA extreme-ultraviolet observations—implications for particle production. *Astrophys. J. Lett.* **733**(2), L25. DOI. ADS.

Kuhn, J.R., Coulter, R., Lin, H., Mickey, D.L.: 2003, The SOLARC off-axis coronagraph. In: Keil, S.L., Avakyan, S.V. (eds.) *Innovative Telescopes and Instrumentation for Solar Astrophysics*, *SPIE C.S.* **4853**, 318. DOI. ADS.

Landi, E., Habbal, S.R., Tomczyk, S.: 2016, Coronal plasma diagnostics from ground-based observations. *J. Geophys. Res.* **121**(9), 8237. DOI. ADS.

Landi, E., Raymond, J.C., Miralles, M.P., Hara, H.: 2010, Physical conditions in a coronal mass ejection from Hinode, STEREO, and SOHO observations. *Astrophys. J.* **711**(1), 75. DOI. ADS.

Landi, E., Hutton, R., Brage, T., Li, W.: 2020, Hinode/EIS measurements of active-region magnetic fields. *Astrophys. J.* **904**(2), 87. DOI. ADS.

Lee, J.-Y., Raymond, J.C., Reeves, K.K., Shen, C., Moon, Y.-J., Kim, Y.-H.: 2019, Nonequilibrium ionization effects on solar EUV and X-ray imaging observations. *Astrophys. J.* **879**(2), 111. DOI. ADS.

Lemen, J.R., Title, A.M., Akin, D.J., Boerner, P.F., Chou, C., Drake, J.F., Duncan, D.W., Edwards, C.G., Friedlaender, F.M., Heyman, G.F., Hurlburt, N.E., Katz, N.L., Kushner, G.D., Levay, M., Lindgren, R.W., Mathur, D.P., McFeaters, E.L., Mitchell, S., Rehse, R.A., Schrijver, C.J., Springer, L.A., Stern, R.A., Tarbell, T.D., Wuelser, J.-P., Wolfson, C.J., Yanari, C., Bookbinder, J.A., Cheimets, P.N., Caldwell, D., Deluca, E.E., Gates, R., Golub, L., Park, S., Podgorski, W.A., Bush, R.I., Scherrer, P.H., Gummin, M.A., Smith, P., Auker, G., Jerram, P., Pool, P., Soufli, R., Windt, D.L., Beardsley, S., Clapp, M., Lang, J., Waltham, N.: 2012, The Atmospheric Imaging Assembly (AIA) on the Solar Dynamics Observatory (SDO). *Solar Phys.* **275**(1-2), 17. DOI. ADS.

Lepping, R.P., Argentiero, P.D.: 1971, Single spacecraft method of estimating shock normals. *J. Geophys. Res.* **76**(19), 4349. DOI. ADS.

Li, H., Landi Degl'Innocenti, E., Qu, Z.: 2017, Polarization of coronal forbidden lines. *Astrophys. J.* **838**(1), 69. DOI. ADS.

Li, W., Grumer, J., Yang, Y., Brage, T., Yao, K., Chen, C., Watanabe, T., Jönsson, P., Lundstedt, H., Hutton, R., Zou, Y.: 2015, A novel method to determine magnetic fields in low-density plasma facilitated through accidental degeneracy of quantum states in Fe^{9+}. *Astrophys. J.* **807**(1), 69. DOI. ADS.

Li, W., Yang, Y., Tu, B., Xiao, J., Grumer, J., Brage, T., Watanabe, T., Hutton, R., Zou, Y.: 2016, Atomic-level pseudo-degeneracy of atomic levels giving transitions induced by magnetic fields, of importance for determining the field strengths in the solar corona. *Astrophys. J.* **826**(2), 219. DOI. ADS.

Lin, H., Kuhn, J.R., Coulter, R.: 2004, Coronal magnetic field measurements. *Astrophys. J. Lett.* **613**(2), L177. DOI. ADS.

Lin, H., Penn, M.J., Tomczyk, S.: 2000, A new precise measurement of the coronal magnetic field strength. *Astrophys. J. Lett.* **541**(2), L83. DOI. ADS.

Lin, J., Ko, Y.-K., Sui, L., Raymond, J.C., Stenborg, G.A., Jiang, Y., Zhao, S., Mancuso, S.: 2005, Direct observations of the magnetic reconnection site of an eruption on 2003 November 18. *Astrophys. J.* **622**(2), 1251. DOI. ADS.

Lionello, R., Linker, J.A., Mikić, Z.: 2009, Multispectral emission of the sun during the first whole sun month: magnetohydrodynamic simulations. *Astrophys. J.* **690**(1), 902. DOI. ADS.

Liu, Y., Luhmann, J.G., Bale, S.D., Lin, R.P.: 2009, Relationship between a coronal mass ejection-driven shock and a coronal metric type II burst. *Astrophys. J. Lett.* **691**(2), L151. DOI. ADS.

Ma, S., Raymond, J.C., Golub, L., Lin, J., Chen, H., Grigis, P., Testa, P., Long, D.: 2011, Observations and interpretation of a low coronal shock wave observed in the EUV by the SDO/AIA. *Astrophys. J.* **738**(2), 160. DOI. ADS.

Mickey, D.L.: 1973, Polarization measurements in the green coronal line. *Astrophys. J. Lett.* **181**, L19. DOI. ADS.

Mikić, Z., Downs, C., Linker, J.A., Caplan, R.M., Mackay, D.H., Upton, L.A., Riley, P., Lionello, R., Török, T., Titov, V.S., Wijaya, J., Druckmüller, M., Pasachoff, J.M., Carlos, W.: 2018, Predicting the corona for the 21 August 2017 total solar eclipse. *Nat. Astron.* **2**, 913. DOI. ADS.

Nakariakov, V.M., Ofman, L.: 2001, Determination of the coronal magnetic field by coronal loop oscillations. *Astron. Astrophys.* **372**, L53. DOI. ADS.

O'Dwyer, B., Del Zanna, G., Mason, H.E., Weber, M.A., Tripathi, D.: 2010, SDO/AIA response to coronal hole, quiet sun, active region, and flare plasma. *Astron. Astrophys.* **521**, A21. DOI. ADS.

Pesnell, W.D., Thompson, B.J., Chamberlin, P.C.: 2012, The Solar Dynamics Observatory (SDO). *Solar Phys.* **275**(1–2), 3. DOI. ADS.

Querfeld, C.W.: 1977, Observations of Fe XIII 10747 coronal emission-line polarization. *Rep. Obs. Lund* **12**, 109. ADS.

Rachmeler, L.A., Gibson, S.E., Dove, J.B., DeVore, C.R., Fan, Y.: 2013, Polarimetric properties of flux ropes and sheared arcades in coronal prominence cavities. *Solar Phys.* **288**(2), 617. DOI. ADS.

Raghavendra Prasad, B., Banerjee, D., Singh, J., Nagabhushana, S., Kumar, A., Kamath, P.U., Kathiravan, S., Venkata, S., Rajkumar, N., Natarajan, V., Juneja, M., Somu, P., Pant, V., Shaji, N., Sankarsubramanian, K., Patra, A., Venkateswaran, R., Adoni, A.A., Narendra, S., Haridas, T.R., Mathew, S.K., Mohan Krishna, R., Amareswari, K., Jaiswal, B.: 2017, Visible emission line coronagraph on Aditya-L1. *Curr. Sci.* **113**(4), 613. DOI. ADS.

Raouafi, N.E., Riley, P., Gibson, S., Fineschi, S., Solanki, S.K.: 2016, Diagnostics of coronal magnetic fields through the Hanle effect in UV and IR lines. *Front. Astron. Space Sci.* **3**, 20. DOI. ADS.

Reginald, N., Newmark, J., Rastaetter, L.: 2020, Synoptic measurements of electron temperature and speed in the solar corona with next generation white-light coronagraph. *Solar Phys.* **295**(7), 95. DOI. ADS.

Rimmele, T.R., Warner, M., Keil, S.L., Goode, P.R., Knölker, M., Kuhn, J.R., Rosner, R.R., McMullin, J.P., Casini, R., Lin, H., Wöger, F., von der Lühe, O., Tritschler, A., Davey, A., de Wijn, A., Elmore, D.F., Fehlmann, A., Harrington, D.M., Jaeggli, S.A., Rast, M.P., Schad, T.A., Schmidt, W., Mathioudakis, M., Mickey, D.L., Anan, T., Beck, C., Marshall, H.K., Jeffers, P.F., Oschmann, J.M., Beard, A., Berst, D.C., Cowan, B.A., Craig, S.C., Cross, E., Cummings, B.K., Donnelly, C., de Vanssay, J.-B., Eigenbrot, A.D., Ferayorni, A., Foster, C., Galapon, C.A., Gedrites, C., Gonzales, K., Goodrich, B.D., Gregory, B.S., Guzman, S.S., Guzzo, S., Hegwer, S., Hubbard, R.P., Hubbard, J.R., Johansson, E.M., Johnson, L.C., Liang, C., Liang, M., McQuillen, I., Mayer, C., Newman, K., Onodera, B., Phelps, L., Puentes, M.M., Richards, C., Rimmele, L.M., Sekulic, P., Shimko, S.R., Simison, B.E., Smith, B., Starman, E., Sueoka, S.R., Summers, R.T., Szabo, A., Szabo, L., Wampler, S.B., Williams, T.R., White, C. (eds.): 2020, The Daniel K. Inouye solar telescope – observatory overview. *Solar Phys.* **295**(12), 172. DOI. ADS.

Sahal-Brechot, S.: 1977, Calculation of the polarization degree of the infrared lines of Fe XIII of the solar corona. *Astrophys. J.* **213**, 887. DOI. ADS.

Scherrer, P.H., Bogart, R.S., Bush, R.I., Hoeksema, J.T., Kosovichev, A.G., Schou, J., Rosenberg, W., Springer, L., Tarbell, T.D., Title, A., Wolfson, C.J., Zayer, I., MDI Engineering Team: 1995, The solar oscillations investigation – Michelson Doppler imager. *Solar Phys.* **162**(1–2), 129. DOI. ADS.

Scherrer, P.H., Schou, J., Bush, R.I., Kosovichev, A.G., Bogart, R.S., Hoeksema, J.T., Liu, Y., Duvall, T.L., Zhao, J., Title, A.M., Schrijver, C.J., Tarbell, T.D., Tomczyk, S.: 2012, The Helioseismic and Magnetic Imager (HMI) investigation for the Solar Dynamics Observatory (SDO). *Solar Phys.* **275**(1–2), 207. DOI. ADS.

Schmelz, J.T., Reames, D.V., von Steiger, R., Basu, S.: 2012, Composition of the solar corona, solar wind, and solar energetic particles. *Astrophys. J.* **755**(1), 33. DOI. ADS.

Schmit, D.J., Gibson, S.E., Tomczyk, S., Reeves, K.K., Sterling, A.C., Brooks, D.H., Williams, D.R., Tripathi, D.: 2009, Large-scale flows in prominence cavities. *Astrophys. J. Lett.* **700**(2), L96. DOI. ADS.

Schrijver, C.J.: 2015, Socio-economic hazards and impacts of space weather: the important range between mild and extreme. *Space Weather* **13**(9), 524. DOI. ADS.

Seetha, S., Megala, S.: 2017, Aditya-L1 mission. *Curr. Sci.* **113**(4), 610. DOI. ADS.

Su, W., Li, T.M., Cheng, X., Feng, L., Zhang, P.J., Chen, P.F., Ding, M.D., Chen, L.J., Guo, Y., Wang, Y., Li, D., Zhang, L.Y.: 2022, Quantifying the magnetic structure of a coronal shock producing a type II radio burst. *Astrophys. J.* **929**(2), 175. DOI. ADS.

Thompson, B.J., Plunkett, S.P., Gurman, J.B., Newmark, J.S., St. Cyr, O.C., Michels, D.J.: 1998, SOHO/EIT observations of an Earth-directed coronal mass ejection on May 12, 1997. *Geophys. Res. Lett.* **25**(14), 2465. DOI. ADS.

Tian, H., McIntosh, S.W., Xia, L., He, J., Wang, X.: 2012, What can we learn about solar coronal mass ejections, coronal dimmings, and extreme-ultraviolet jets through spectroscopic observations? *Astrophys. J.* **748**(2), 106. DOI. ADS.

Tian, H., Tomczyk, S., McIntosh, S.W., Bethge, C., de Toma, G., Gibson, S.: 2013, Observations of coronal mass ejections with the coronal multichannel polarimeter. *Solar Phys.* **288**(2), 637. DOI. ADS.

Titov, V.S., Török, T., Mikic, Z., Linker, J.A.: 2014, A method for embedding circular force-free flux ropes in potential magnetic fields. *Astrophys. J.* **790**(2), 163. DOI. ADS.

Tomczyk, S., Landi, E.: 2019, Upgraded coronal multi-channel polarimeter (UCoMP). In: *Solar Heliospheric and INterplanetary Environment (SHINE 2019)*, 131. ADS.

Tomczyk, S., Card, G.L., Darnell, T., Elmore, D.F., Lull, R., Nelson, P.G., Streander, K.V., Burkepile, J., Casini, R., Judge, P.G.: 2008, An instrument to measure coronal emission line polarization. *Solar Phys.* **247**(2), 411. DOI. ADS.

Tomczyk, S., Landi, E., Burkepile, J.T., Casini, R., DeLuca, E.E., Fan, Y., Gibson, S.E., Lin, H., McIntosh, S.W., Solomon, S.C., Toma, G., Wijn, A.G., Zhang, J.: 2016, Scientific objectives and capabilities of the coronal solar magnetism observatory. *J. Geophys. Res.* **121**(8), 7470. DOI. ADS.

Török, T., Downs, C., Linker, J.A., Lionello, R., Titov, V.S., Mikić, Z., Riley, P., Caplan, R.M., Wijaya, J.: 2018, Sun-to-Earth MHD simulation of the 2000 July 14 "Bastille Day" eruption. *Astrophys. J.* **856**(1), 75. DOI. ADS.

Vourlidas, A., Howard, R.A., Esfandiari, E., Patsourakos, S., Yashiro, S., Michalek, G.: 2010, Comprehensive analysis of coronal mass ejection mass and energy properties over a full solar cycle. *Astrophys. J.* **722**(2), 1522. DOI. ADS.

Vourlidas, A., Lynch, B.J., Howard, R.A., Li, Y.: 2013, How many CMEs have flux ropes? Deciphering the signatures of shocks, flux ropes, and prominences in coronagraph observations of CMEs. *Solar Phys.* **284**(1), 179. DOI. ADS.

Wang, Y.M., Ye, P.Z., Wang, S., Zhou, G.P., Wang, J.X.: 2002, A statistical study on the geoeffectiveness of Earth-directed coronal mass ejections from March 1997 to December 2000. *J. Geophys. Res.* **107**(A11), 1340. DOI. ADS.

Webb, D.F., Howard, T.A.: 2012, Coronal mass ejections: observations. *Living Rev. Solar Phys.* **9**(1), 3. DOI. ADS.

Xu, Y., Tian, H., Hou, Z., Yang, Z., Gao, Y., Bai, X.: 2022, Sun-as-a-star spectroscopic observations of the line-of-sight velocity of a solar eruption on 2021 October 28. *Astrophys. J.* **931**(2), 76. DOI. ADS.

Yang, Z., Bethge, C., Tian, H., Tomczyk, S., Morton, R., Del Zanna, G., McIntosh, S.W., Karak, B.B., Gibson, S., Samanta, T., He, J., Chen, Y., Wang, L.: 2020a, Global maps of the magnetic field in the solar corona. *Science* **369**(6504), 694. DOI. ADS.

Yang, Z., Tian, H., Tomczyk, S., Morton, R., Bai, X., Samanta, T., Chen, Y.: 2020b, Mapping the magnetic field in the solar corona through magnetoseismology. *Sci. China, Technol. Sci.* **63**(11), 2357. DOI. ADS.

Yashiro, S., Gopalswamy, N., Michalek, G., St. Cyr, O.C., Plunkett, S.P., Rich, N.B., Howard, R.A.: 2004, A catalog of white light coronal mass ejections observed by the SOHO spacecraft. *J. Geophys. Res.* **109**(A7), A07105. DOI. ADS.

Ying, B., Bemporad, A., Giordano, S., Pagano, P., Feng, L., Lu, L., Li, H., Gan, W.: 2019, First determination of 2D speed distribution within the bodies of coronal mass ejections with cross-correlation analysis. *Astrophys. J.* **880**(1), 41. DOI. ADS.

Young, M.A., Schwadron, N.A., Gorby, M., Linker, J., Caplan, R.M., Downs, C., Török, T., Riley, P., Lionello, R., Titov, V., Mewaldt, R.A., Cohen, C.M.S.: 2021, Energetic proton propagation and acceleration simulated for the Bastille Day event of 2000 July 14. *Astrophys. J.* **909**(2), 160. DOI. ADS.

Zhao, J., Gibson, S.E., Fineschi, S., Susino, R., Casini, R., Li, H., Gan, W.: 2019, Simulating the solar corona in the forbidden and permitted lines with forward modeling. I. Saturated and unsaturated hanle regimes. *Astrophys. J.* **883**(1), 55. DOI. ADS.

Zhao, J., Gibson, S.E., Fineschi, S., Susino, R., Casini, R., Cranmer, S.R., Ofman, L., Li, H.: 2021, Simulating the solar minimum corona in UV wavelengths with forward modeling II. Doppler dimming and microscopic anisotropy effect. *Astrophys. J.* **912**(2), 141. DOI. ADS.

Zhou, G., Wang, Y., Wang, J.: 2006, Coronal mass ejections associated with polar crown filaments. *Adv. Space Res.* **38**(3), 466. DOI. ADS.

Publisher's Note Springer Nature remains neutral with regard to jurisdictional claims in published maps and institutional affiliations.

Springer Nature or its licensor (e.g. a society or other partner) holds exclusive rights to this article under a publishing agreement with the author(s) or other rightsholder(s); author self-archiving of the accepted manuscript version of this article is solely governed by the terms of such publishing agreement and applicable law.